electronics

MDPI

Review

Heterostructure-Based Optoelectronic Neuromorphic Devices

Jisoo Park, Jihyun Shin and Hocheon Yoo *

Department of Electronic Engineering, Gachon University, Seongnam 13120, Republic of Korea
* Correspondence: hyoo@gachon.ac.kr

Abstract: The concept of neuromorphic devices, aiming to process large amounts of information in parallel, at low power, high speed, and high efficiency, is to mimic the functions of human brain by emulating biological neural behavior. Optoelectronic neuromorphic devices are particularly suitable for neuromorphic applications with their ability to generate various pulses based on wavelength and to control synaptic stimulation. Each wavelength (ultraviolet, visible, and infrared) has specific advantages and optimal applications. Here, the heterostructure-based optoelectronic neuromorphic devices are explored across the full wavelength range (ultraviolet to infrared) by categorizing them on the basis of irradiated wavelength and structure (two-terminal and three-terminal) with respect to emerging optoelectrical materials. The relationship between neuromorphic applications, light wavelength, and mechanism is revisited. Finally, the potential and challenging aspects of next-generation optoelectronic neuromorphic devices are presented, which can assist in the design of suitable materials and structures for neuromorphic-based applications.

Keywords: heterostructure; optoelectronics; neuromorphic devices; synaptic devices; visual sensors

Citation: Park, J.; Shin, J.; Yoo, H. Heterostructure-Based Optoelectronic Neuromorphic Devices. *Electronics* **2024**, *13*, 1076. https://doi.org/10.3390/electronics13061076

Academic Editors: Elias Stathatos and Spyros N. Yannopoulos

Received: 29 January 2024
Revised: 7 March 2024
Accepted: 8 March 2024
Published: 14 March 2024

1. Introduction

Neuromorphic devices aim to mimic the high-level functions of the human brain, requiring the emulation of the operational principles of biological neural behavior [1–3], which can be achieved through the modulation of connections between neurons and the strength of synapses [4]. Key features that neuromorphic devices should possess for this purpose include plasticity [5–7], linearity [8–10], symmetry [8,10,11], and accordingly extremely low power consumption [12–15] and highly efficient operation. As one candidate for these neuromorphic devices, optoelectronic devices have the potential to provide artificial systems capable of reproducing the structure and functions of the human brain. The combination of electronic devices and their procedures forms an efficient processing information format, similar to the neurons in an organic brain [16–18]. This optoelectronic device, alongside artificial intelligence, provides both optical and electronic advantages within a single device to enhance adaptability, reconstruct images, and process information efficiently [19]. Furthermore, light provides the advantage of generating a wide range of light pulses based on wavelength, making it highly suitable for synaptic stimulation control inputs. To be specific, light is capable of generating photo-excited carriers (i.e., hole and electron pairs) based on intensity and wavelength, offering precise modulation for opto-stimulated plasticity [20–22].

Light has respective applications depending on different wavelengths (i.e., ultraviolet, visible, and infrared) [23–25], each with its advantages and disadvantages [26–31]. For example, ultraviolet (UV) light, due to its large bandgap in absorption materials, is relatively noise-free compared to other wavelengths [32,33]. Visible light is advantageous for image sensing and biological modeling, as it is the wavelength most extensively utilized in human and animal vision [23,34,35]. Infrared (IR) light enables traveling through relatively long distances [36,37] and safe operation of near-human devices [38–40]. Accordingly, the implementation of optoelectronic neuromorphic devices depending on the wavelength

of light can have specific purposes for each, suggesting the development of customized directions for applications.

Meanwhile, heterostructure (i.e., heterojunction) refers to the interface between two different material layers, in which these materials have different energy band structures, and accordingly, energy bandgaps [41–43]. With respect to the optoelectronic property aspect, due to the disparate energy band junction, an additional photoelectric effect or photogating effect can be obtained by means of the energy band alignment structure [44–49]. Thus, the benefits of heterostructures include an improved photo-response resulting from the junction structure with energy band differences, a versatility that allows application in various scenarios based on different combinations, and the ability to explore expandable or controllable wavelength ranges depending on the combination of the chosen materials.

In this context, we explored heterostructure-based optoelectronic neuromorphic devices and their applications by investigating the full wavelength range of light from UV to IR. Section 2 first summarizes the fundamental biological synaptic functions. In Section 3, we introduce the current state-of-the-art research on optoelectronic neuromorphic devices based on heterostructures. The devices are classified into irradiated wavelength, and more specifically, according to their structure (i.e., two-terminal and three-terminal) [50–52]. As the light wavelength of choice and the mechanism of the device determine synaptic properties and application of the device additionally to the gate voltage (V_G) bias, this new perspective reveals the relationship between various neuromorphic applications and the wavelength and mechanism of irradiated light. Therefore, this paper is expected to help the process of exploring and designing appropriate materials and structures when neuromorphic-based applications are first considered for research purposes.

2. Fundamental Functionalities of Neuromorphic Devices Mimicking Biological Synapse

The human neural network consists of neurons, which are nerve cells, and synapses, which are junctions between neurons where signals are transmitted from the presynaptic neuron to the postsynaptic neuron across the synapse. The transmission, processing, and storage of information rely on the mechanism of synaptic plasticity [7,53,54], whereby connections between nerves are strengthened or weakened when external stimuli in the form of electrical or chemical pulses are applied. These processes are carried out in a low-power, high-speed, and highly efficient manner. For the neuromorphic devices, synaptic plasticity is usually implemented by current or conductivity [55–57].

2.1. Excitatory Postsynaptic Current (EPSC)/Inhibitory Postsynaptic Current (IPSC)

When an input neuron device emits a presynaptic signal corresponding to a presynaptic neuron, an output neuron device generates a postsynaptic signal according to the synaptic weight (conductance). The resulting electrical signal generated by the postsynaptic neuron is called an excitatory postsynaptic current (EPSC) or inhibitory postsynaptic current (IPSC). The value of EPSC/IPSC is proportional to the weight changes, with a higher EPSC/IPSC value implying a stronger weight change in the synaptic plasticity [58]. EPSCs/IPSCs are the most basic synaptic mechanisms for transmitting, processing, and storing information in the biological nervous system [59–62].

2.2. Short-Term Plasticity (STP)/Long-Term Plasticity (LTP)

The difference between short-term plasticity (STP) and long-term plasticity (LTP) is retention time. STP is a transient change in synaptic weight that can only last up to a few seconds before returning to its original state, whereas LTP can last for years or transfer into permanent memory [55,63]. STP could be converted to LTP as a learning process with repeated training and rehearsals [58,64–68].

2.3. Paired-Pulse Facilitation (PPF)/Paired-Pulse Depression (PPD)

Paired-pulse facilitation (PPF) and pair-pulse depression (PPD) are specific forms of short-term plasticity behavior, which are important for recognizing and decoding temporal information. The PPF/PPD is defined as the increased/decreased ratio between the two consecutive EPSC, indicating reinforced or weakened post-synaptic signal by the following spike. It depends on the various parameters such as pulse width, intensity, and interval [3,69–71].

2.4. Spike-Time-Dependent Plasticity (STDP)/Spike-Rate-Dependent Plasticity (SRDP)

Spike-time-dependent plasticity (STDP) and spike-rate-dependent plasticity (SRDP) are the typical long-term plasticities, and are two examples of the Hebbian learning rule. STDP shows the correlation of synaptic plasticity between presynaptic and postsynaptic signals by their order and time intervals ($\Delta t = t_{pre} - t_{post}$). LTP has occurred when the presynaptic spike occurs earlier than the postsynaptic spike ($\Delta t > 0$). Conversely, LTD happens when the presynaptic spike occurs later than the postsynaptic spike ($\Delta t < 0$). As the time interval increases, the synaptic weight changes as the influence of the two signals on each other changes, and the synaptic plasticity can be anticipated by the STDP curve from the known time interval [55]. Meanwhile, SRDP shows the dependency of synaptic plasticity according to the frequency of the spikes [11,72–74].

2.5. Potentiation/Depression

Synaptic plasticity can be described as either potentiation or depression, depending on the shape of the pulse. Potentiation refers to an overall increase in synaptic weight with pulse number (signal strengthening). On the other hand, depression refers to the successive decrease in synaptic weight as a function of pulse number (signal weakening) [75–79].

3. Heterostructure-Based Optoelectronic Neuromorphic Devices Using Various Wavelength of Light

3.1. Optoelectronic Neuromorphic Devices Using UV Light

UV light is widely used as an optical stimulation onto various optoelectronic devices for its non-disturbed optical properties derived from the wide band gap of the light absorbing materials. Due to the high energy level UV light possesses, UV illumination can provide an optoelectronic neuromorphic device with stable operation, noise-free performance, and other advantages from overwhelming other unwantedly induced optical disturbances from longer wavelength ranges. Thus, we collected UV-utilizing optoelectronic neuromorphic studies where they specifically selected materials and designed device structures for UV reaction for the mentioned merits.

In 2023, Guo et al. published a study on an optoelectronic device where the heterostructures of PI and graphene were used for mimicking the neuromorphic function of rod and cone cells in a human brain (Figure 1a) [80]. External stimuli were given in the forms of 365 nm UV light and negative gas ions induced by triboelectric nanogenerator (TENG). Where TENG-induced gas ions act as a negatively charged floating gate by being adsorbed onto a graphene surface, PI generates photocurrent under UV light illumination, while also functioning as a flexible substrate for a CVD-grown monolayer graphene channel. The CVD method of graphene fabrication creates defects in graphene, making a p-type doping effect to enable hole carrier conduction. As depicted in Figure 1b, electrons from UV light-induced electron-hole pairs can slowly traverse from the PI surface into the graphene channel and recombine with holes in defect sites of graphene, ultimately leading to a reduction in the total hole current. The structural design and material selection resulted in negative photoconductance phenomenon, where PI was selected for its non-conductive and UV-absorbing properties, while graphene plays the exact opposite role of high-conductance and low absorbance derived from its zero-band gap. The negative photoconductance was used to optically demonstrate LTD of the device (Figure 1c) and synaptic image sensing of a handwritten digit which achieved 84% accuracy at its highest.

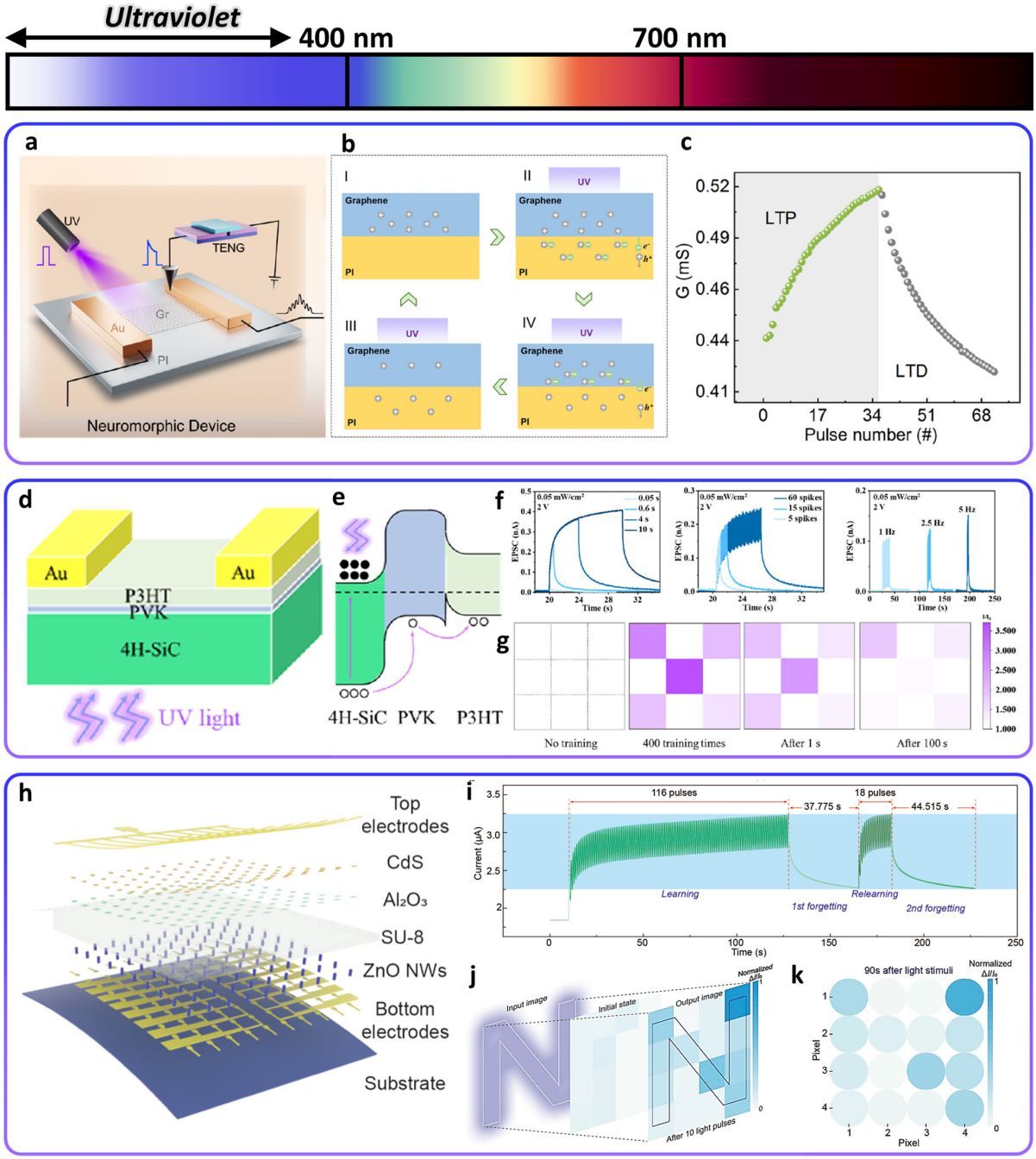

Figure 1. (**a**) A schematic illustration of graphene/PI neuromorphic device (**b**) and its optoelectronic behavior under UV light ((I) the original state, (II) photo-induced carrier generation, (III) carrier transport between layers and (IV) the final state after recombination). (**c**) Demonstrated LTP and LTD behavior of the device. (**d**) A schematic illustration of P3HT/PVK/4H-SiC synaptic transistor. (**e**) A schematic illustration of synaptic weight generation by UV light. (**f**) Optically obtained EPSC plots by consecutive UV spikes with different spike duration, number, and frequency. (**g**) Learning and forgetting process from pattern recognition. (**h**) Schematic illustration of the ZAC-OSs-based device structure. (**i**) PPC effect after irradiating UV light with intensity of 5.0 Mw·cm^{-2}. (**j**) The modulated synaptic learning behavior by piezo-phototronic effect under UV light pulse. (**k**) Demonstration of array memorizing image after input with 10 UV light pulses. (**a**–**c**) Reproduced with permission from [80]. Copyright Elsevier, 2023. (**d**–**g**) Reproduced with permission from [81]. Copyright American Chemical Society, 2023. (**h**–**k**) Reproduced with permission from [58]. Copyright Wiley, 2023.

A study by Liu et al. in 2023 presented a photogated synaptic transistor for neuromorphic UV vision, using heterostructures of 4H-SiC and p-type organic semiconductors, including PVK and P3HT (Figure 1d) [81]. The main absorption of UV happens in the 4H-SiC layer, while PVK and P3HT serve as p-type channels due to their high hole mobility. Figure 1e illustrates the band energy diagram, where 4H-SiC creates photocarriers under UV irradiation of 375 nm wavelength. Electrons remain in 4H-SiC blocked by high conduction band level of PVK, and holes transfer into P3HT, owing to the hole-conducting and electron-trapping characteristics in the energy band structure of PVK. Separating photo-generated electron-hole pairs into different layers of the device slows down the recombination process, thereby increasing conductance and inducing LTP behavior by irradiation of UV light pulse (Figure 1f). An image of the letter "X" was put through a demonstration process to mimic biological learning and forgetting (Figure 1g), which showed clear image recognition after 400 training instances, followed by gradual decay.

Han et al. mimicked the human visual-perception system by simply fabricating a two-terminal ZnO/Al_2O_3/CdS heterojunction-based optoelectronic synapses (ZAC-OSs) array in 2023 (Figure 1h) [58]. An instant increase and a gradual decay in photocurrent after irradiating and removing the 365 nm of UV light occurred due to the PPC behavior of ZnO nanowires (NWs) and CdS film. Therefore, a concept of "learning-experience" was achieved by UV light (2.48 mW·cm^{-2}, duration: 0.5 s) stimulation with various frequencies and pulse numbers, allowing short-term memory (STM) to transition to long-term memory (LTM). Interestingly, additional external strain induced slower facilitation and decay tendency of the PPF index due to the piezo-phototronic effect (Figure 1i), modulating synaptic weight in multilevel and reinforcing memorization of the device. When 'N' shaped UV light stimulation (pulse width: 0.5 s, frequency: 1 Hz, and intensity: 2.48 mW·cm^{-2}) and 24.5 MPa external compression pressure were applied from the bottom and top of the substrate, respectively, it stored an 'N' shaped image for 90 s (Figure 1j,k). The recognition rate of 99.68% could be achieved with the help of an artificial neural network (ANN).

A device in the study of Ni et al., 2021, demonstrated a photoelectric neuromorphic transistor (PENT) with ZnO NWs, 2,7-Dioctyl [1]benzothieno[3,2-b][1]benzothiophene (C8-BTBT), and poly(methyl methacrylate) (PMMA) [82]. ZnO NWs were covered by 2D phase-separated PMMA/C-BTBT film. As shown in Figure 2a, this structure imitates the biological optical sensing neuron with quasi-one-dimensional materials sparsely covered by two-dimensional materials. Since ZnO and C8-BTBT have significant absorption in UV wavelengths, both layers generate photo-excited electron-hole pairs under irradiation interleaving a thin PMMA insulating layer between them. Due to their energy band aligning position, photo-generated electrons tunnel through PMMA from C8-BTBT into ZnO, while holes reversely tunnel from ZnO into C8-BTBT (Figure 2b). This asymmetric distribution of photocarrier charge effectively impedes carrier recombination and current level decay after optical stimuli, alongside ZnO oxygen vacancy and PMMA film acting as trapping sites. An applicational demonstration was made with a 64 × 64 PENT array and a shadow mask, where UV light of 380 nm wavelength was irradiated through the shadow mask for 3.5 s. The irradiated devices detected and memorized the patterned image as a result of increased synaptic weight, with slight losses after 2 h.

In 2021, Ahmed et al. designed a hetero-structured device (Figure 2c) with black phosphorus (BP), which exhibits unique photo-response properties in range of UV light wavelengths [83]. The BP channel proved to have a naturally formed thin layer of phosphorus oxide (P_xO_x) both on top and under the BP flake layer. While performing as a self-passivation layer, this oxidized surface is also believed to create negative photoconductance with optical carrier excitation, dissociating ambient adsorbates with optical energy, hence increasing the total amount of trap sites for charge transfer. Thus, the device fabrication process was thermally controlled to have native P_xO_x, to intentionally create negative photoconductance phenomenon. In the results in Figure 2d, the BP transistor device showed decreasing photocurrent when irradiated with 365 nm UV pulse, whereas irradiation of 280 nm light pulse generated increasing photocurrent, which is rendered

from providing sufficient energy for the ambient hydrogen to be adsorbed onto defect sites and passivate the surface, eventually raising carrier concentration in the BP channel. Utilizing these optoelectrical properties of BP, the team demonstrated fully light-controlled LTP and LTD with 280 nm and 365 UV irradiation, respectively (Figure 2e), which was also applied to optical memory operation and image recognition.

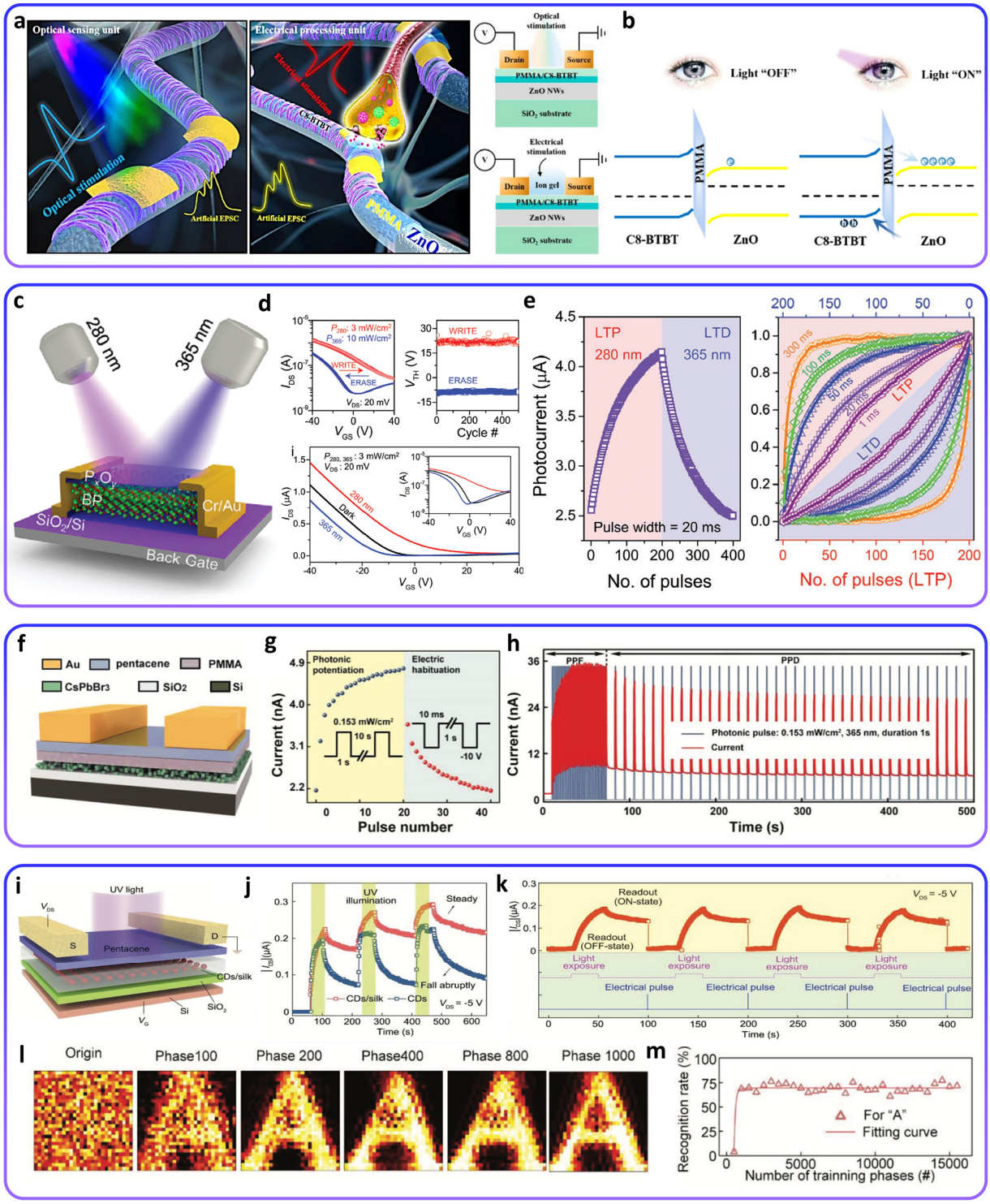

Figure 2. (**a**) A schematic image of optical neurons and neuromorphic phototransistor based on C8-BTBT and ZnO NWs. (**b**) Band diagram image under dark and light conditions. (**c**) A schematic image of BP neuromortphic phototransistor. (**d**) Optical write and erase states by 280 nm and 365 nm

irradiation, respectively. (**e**) Graphs of optically induced LTP and LTD. (**f**) Schematic illustration of the flash memory device based on $CsPbBr_3$ QDs. (**g**) Photonic potentiation and electric habituation behavior of the $CsPbBr_3$ QD device. (**h**) PPD afger PPF experimentally demonstrated by the memory device. (**i**) Schematic illustration of the optical flash memory device based on CDs/silk heterostructure. (**j**) Transient characteristics of CDs/silk-based and CDs-based flash memory device after optical programming. (**k**) Optical and electrical operating sequence and the corresponding readout current of the memory device. (**l**) Original mapping images and (**m**) recognition state of letter "A" with the increasing training phases. (**a**,**b**) Reproduced with permission from [82]. Copyright Elsevier, 2021. (**c**–**e**) Reproduced with permission from [83]. Copyright Wiley, 2020. (**f**–**h**) Reproduced with permission from [63]. Copyright Wiley, 2018. (**i**–**m**) Reproduced with permission from [84]. Copyright Wiley, 2019.

In 2018, Wang et al. set up an optoelectrical synapse with a novel heterostructure of flash memory using solution-processed $CsPbBr_3$ quantum dots (QDs) and pentacene (Figure 2f) [63]. The strong UV light absorption of $CsPbBr_3$ generated excitons and they were separated at the type II heterojunction between pentacene and $CsPbBr_3$ QDs. Accumulated electrons in $CsPbBr_3$ QDs and holes in pentacene layer showed the memory behavior of the device. Both programmed and erased states were maintained for more than 1×10^4 s and for 10^3 cycles without obvious degradation. This memory formation with 365 nm (0.153 $mW \cdot cm^{-2}$, 1 s duration with 10 s interval) of light stimulus and loss with electrical pulses enabled implementation including the transition from STP to LTP, PPF, and SRDP (Figure 2g). Increasing the pulse interval to 10 s, partially detrapped electrons recombined with the holes, showing PPD behavior (Figure 2h).

In a subsequent study in 2019, Lv et al. fabricated an optical transistor synapse with carbon dots/silk protein (CDs/silk) mixture for charge trapping layer (Figure 2i) [84]. A blend form of CDs in silk improved charge storage stability more than CDs-only memory (Figure 2j). The surface of the CDs on the film act as trap sites where photo-generated electrons are trapped. On the other hand, these trapped electrons can easily recombine with adjacent holes in the pentacene layer, inducing a volatile memory characteristic. In this way, the device could repeat the write and erase operation with a 365 nm of light pulse and a −60 V of gate pulse (Figure 2k). Furthermore, a clear shape of the letter "A" with Modified National Institute of Standards and Technology (MNIST) database could be obtained for the pattern recognition simulation, demonstrating 73% accuracy for pattern recognition (Figure 2l,m).

3.2. Optoelectronic Neuromorphic Devices Using Visible Light

Visible light occupies most of the range in the optical wavelength that involves human vision. The ability of many other animals to see also depends mainly on visible light absorption into a retina, from where optical neuron cells detect and process visual inputs. Due to the sophisticated design of biological retina, optoelectronic devices have been endeavoring to catch up to the excellence that the human eye naturally holds, hence imitating its material selection and structural form. The following studies are optoelectronic neuromorphic reports, with various methods and organic semiconductors chosen to realize synaptic operation for visible light detection.

Zhang et al. fabricated a photonic synapse device in 2023, in which $CsPbI_2Br$, a typically perovskite-structured material, was used as a visible light absorbing layer (Figure 3a) [85]. Under visible light stimulation like Figure 3b, $CsPbI_2Br$-generated electron-hole pairs separately traverse into bordering material, functioning as synaptic weights. Due to the high p-type conducting properties, P3HT effectively transports transport holes from $CsPbI_2Br$, while the electrons remain bound to nitrogen-doped graphene quantum dots (N-GQDs). Owing to the well-aligned energy band structures of the whole device materials, the separation of optically excited electrons and holes delays recombination and makes conductivity increase. With an additional aid of a microvoid-structured PMMA layer reducing effective contact area between $CsPbI_2Br$ and P3HT, the device exhibits synaptic

performance including STM and LTM under a light pulse of 470 nm given in intervals, which is in a blue shade visible to human eyes (Figure 3c). The neuromorphic performance of the device was then tested in a 28 × 28 pixels array simulation with handwritten digits recognition, where the maximum accuracy of recognizing large data sets reached 95.99%.

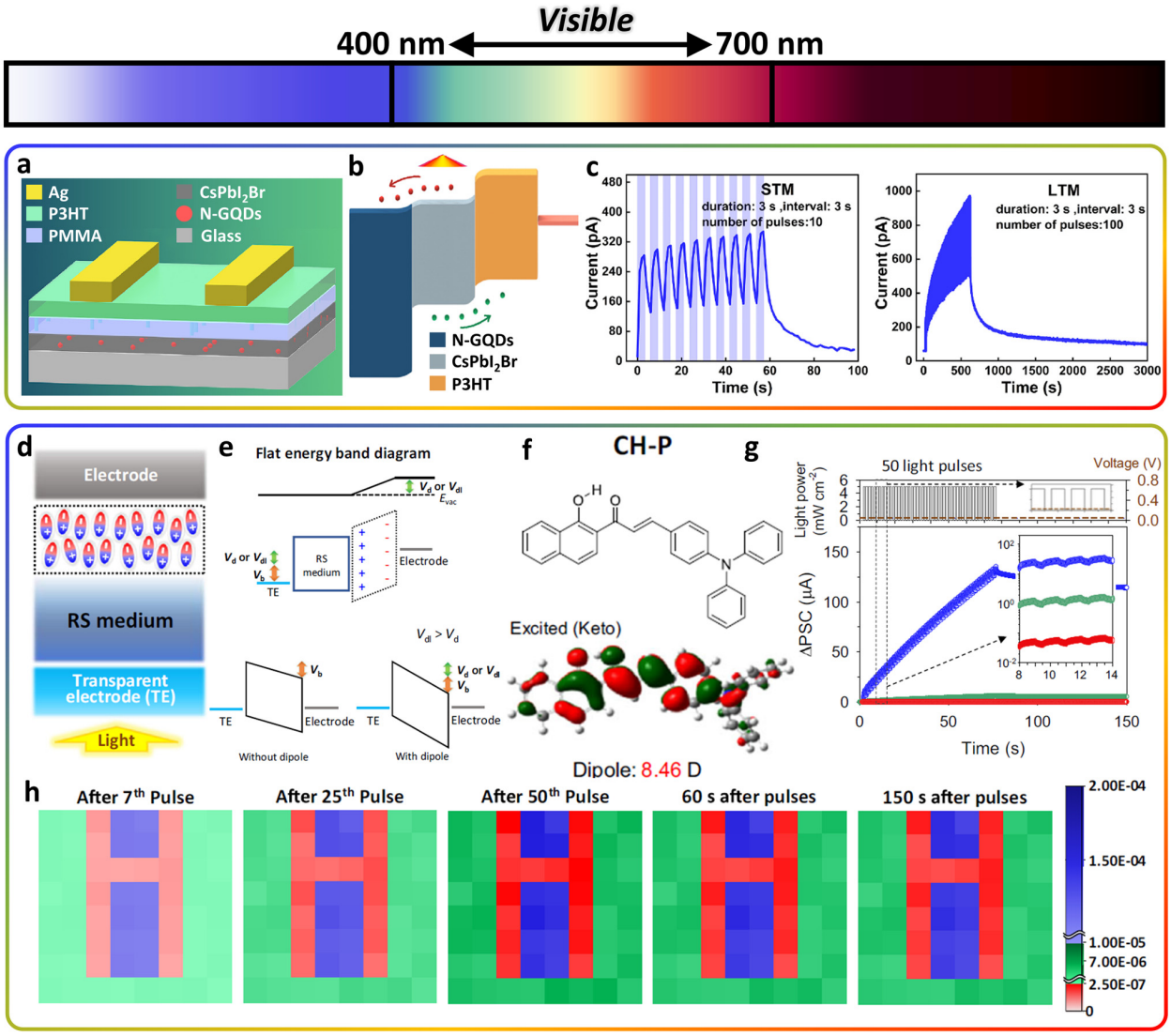

Figure 3. (**a**) A schematic image of two-terminal synaptic device based on $CsPbI_2Br$ and (**b**) generation of synaptic weight generation under illumination. (**c**) Optically induced STM and LTM under 470 nm pulses. (**d**) A schematic image of an organic semiconductor-introduced optoelectronic neuromorphic memristor device. (**e**) Illustrations of energy band diagram without dipole and with dipole. (**f**) A chemical structure of CH-P. (**g**) Optically induced LTP with red, green, and blue lights. (**h**) Demonstration of RGB distinguishing with memristor array. (**a**–**c**) Reproduced with permission from [85]. Copyright Elsevier, 2023. (**d**–**h**) Reproduced with permission from [86]. Copyright American Chemical Society, 2023.

Figure 3d is a schematic illustration of multi color-cognitive neuromorphic memristor reported by Lee et al. in 2023 [86]. The device was fabricated utilizing a thin film of asymmetric-formed organic semiconductor between a switching medium (NiO) and a one-sided transparent electrode (FTO, Ag) for illumination to reach inside. With effective alignment of the intrinsic dipole moment of the organic semiconductor molecules, the accumulation of induced dipole moments can be strong enough so that it modifies the work-function of nearby electrodes, as shown in Figure 3e. To cause these highly accumulative

dipoles, visible light illumination was used to optically excite the organic semiconductor molecules into aligned states. Designing molecules specifically to have photo-tautomerizing characteristics rendered a longer lifetime of the excited state, contributing to the synaptic behavior of the memristor device. A device with blue (450 nm), green (525 nm), and red (630 nm) distinguishing function was made in the form of memristor inserted with (E)-3-(4-(diphenylamino) phenyl)-1-(1-hydroxynaphthalen-2-yl)prop-2-en-1-one (CH-P) (Figure 3f), an organic semiconductor with enhanced visible light absorption. Due to the sharply designed absorption range in visible wavelength, the CH-P integrated 8 × 8 memristor array exhibited synaptic vision with gradual intensity increase (Figure 3g), also successfully recognizing and discriminating RGB pattern under read voltage of 0.05 V (Figure 3h).

In a 2023 study, Wang et al. presented a phototransistor with neuromorphic performance based on a silicon-nanomembrane (Si NM) (Figure 4a) [87]. P3HT was isolated from the electrode with SiO_2 to exclude direct carrier transport between source/drain and Au electrodes, since its high hole mobility overwhelms Si NM and impedes synaptic performance of the device. Additionally, PMMA was used for its passivating ability to obtain stability of lead-sulfide quantum dots (PbS QDs). Due to the electron-blocking feature of P3HT energy band, photo-generated electron-hole pairs in PbS QDs under visible light separate and successfully impart synaptic weight to the device, where holes transfer to P3HT, then Si NM, and electrons remain in trapped states in their originally excited location (Figure 4b). The form of 4 × 5 phototransistor array was used to demonstrate its synaptic learning and forgetting process on visible light, as shown in Figure 4c. A total of 100 optical spikes of both 532 nm and 1342 nm wavelengths were given in different positions to make a pattern, where EPSC with initially detected 1342 nm fades away unrecognizably after 10 s, while stimulation by 532 nm, a green shade visible to human eyes, retains its patterns. Also, a shape of the letter "E" in 11 × 11 array was put through to test EPSC of the synaptic phototransistor devices. Results showed enhancement in memory performance by increasing illuminating duration from 1 s to 10 s, imitating biological relations between stimulating duration and learning process (Figure 4d).

In 2021, Zhu et al. presented a flexible optoelectronic sensor array with carbon nanotubes (CNTs) and $CsPbBr_3$-QDs (Figure 4e) [88]. They acted as an electrical transport and a photon absorption layer, respectively. These materials were chosen to improve photoresponse and signal-to-noise ratio detection, respectively, which in turn showed a high responsivity and specific detectivity of 5.1×10^7 $A \cdot W^{-1}$ and 2×10^{16} Jones, respectively, when irradiated with 405 nm of light (intensity of 48 $\mu W \cdot cm^{-2}$, pulse width of 20 ms). Also, they are suitable for achieving stability, flexibility, and uniform large-scale fabrication. As a result, the device maintained its electrical characteristics even after being stored for more than 8 months in ambient air and bent strains (ε) of 0.4%. The underlying mechanism is a photogating effect that separated holes transfer into the CNT channel while the electrons were trapped in the $CsPbBr_3$-QDs, leading to typical PPF behavior (Figure 4f). Finally, a neuromorphic vision system was implemented with 1024 pixels of sensor array. The calculated recognition accuracy reached 95% after training with 200 pulses under a 405 nm of light (intensity of 1 $\mu W \cdot cm^2$, pulse width of 250 ms, pulse interval of 250 ms) (Figure 4g).

For another $CsPbBr_3$ QDs-based optoelectronic neuromorphic device, Zhang et al. adopted a heterostructure with poly[2,5-(2-octyldodecyl)-3,6-diketopyrrolopyrrole-alt-5,5-(2,5-di(thien-2-yl)thieno [3,2-b]thiophene)] (DPP-DTT) in 2022, which has good air stability and high charge mobility (Figure 4h) [89]. The substrate of ionic conductive cellulose nanopaper (ICCN) enabled the device to operate at low voltage, and at 1 mm bending. The synaptic behavior of PPF was executed with the 450 nm of light pulse (intensity of 0.30 $mW \cdot cm^{-2}$ and Δt of 500 ms) due to the photogating effect. Furthermore, a stronger transition from STP to LTP was observed when a voltage bias ($V_G = -8$ V) was applied in conjunction with the light pulse. The synaptic device showed multibit storage capacity with different photonic pulse durations (Figure 4i). This LTP phenomenon was caused by the removal of the light pulse resulting in a decrease in the carrier recombination rate. The respective features of STP and LTP were utilized to demonstrate 'Morse-code' and visual

object recognition simulation (Figure 4j,k). Additionally, logic functions of "AND", "OR", "NOR", and "NAND" were demonstrated by modulating the inputs with two V_G pulses and photonic pulses (Figure 4l).

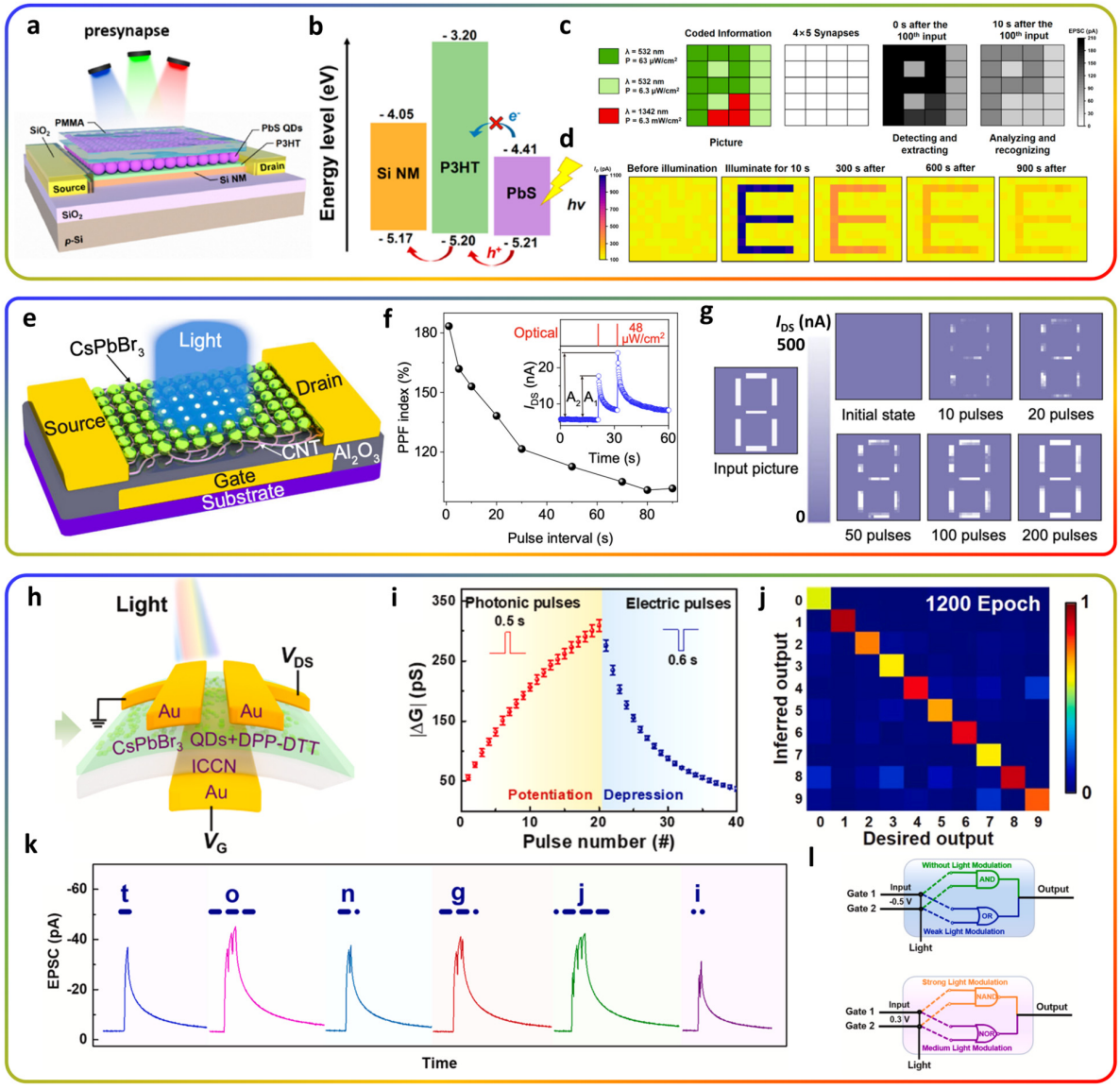

Figure 4. (**a**) A schematic image of organic/inorganic hetero-structured synaptic phototransistor. (**b**) An energy band diagram under visible light stimulus. (**c**) Visible light-recognizing demonstration of the phototransistor array. (**d**) Learning and forgetting process demonstrated by a pattern of letter "E". (**e**) A schematic illustration of the phototransistor device based on CNT and $CsPbBr_3$-QD. (**f**) Gradual decrease of PPF index by pulse interval increase (Inset: PPF achieved by consecutive two optical pulses) (**g**) The input image of "8" pattern and its training weight results from the initial state and after training if 10, 20, 50, 100, and 200 pulses of 405 nm light. (**h**) A schematic illustration of an organic optoelectronic synaptic device based on $CsPbBr_3$ QDs and ICCN. (**i**) Photonic potentiation and electric depression behavior demonstrated by 450 nm photonic pulses and −0.5 V electric gate pulses under the gate voltage of −0.8 V. (**j**) Training results of confusion matrices under the 1200th epoch. (**k**) Morse code of letter "TONGJI" demonstrated by EPSCs induced by a series of photonic 450 nm optical pulses under V_D = −1 V, (**l**) a schematic image of logic circuit demonstration with and without light modulation. (**a**–**d**) Reproduced with permission from [87]. Copyright Nature, 2023. (**e**–**g**) Reproduced with permission from [88]. Copyright Nature, 2021. (**h**–**l**) Reproduced with permission from [89]. Copyright Elsevier, 2022.

3.3. Optoelectronic Neuromorphic Devices Using IR Light

Due to its characteristic of long wavelength, IR vision provides a few animals with the unique abilities of detecting predators or prey from a great distance, signaling each other, and seeing clearly in the visible light-insufficient condition in which other animals would feel completely dark. Also, IR wavelength being outside the detection range of human retina can generate invisible input signals, so that the electronic devices can optically communicate effectively without interfering with human vision. Additionally, IR leaves no risk of possible biological hazard that can occur when using light with shorter energy such as UV wavelength, making it suitable for wearable devices which involve very close range of physical distance with human body. Hence, we review two studies on optoelectronic neuromorphic devices with interesting methods of exploiting IR as an input stimulation.

In 2019, resistive random-access memory (RRAM) based on a quasi-plane $MoSe_2/Bi_2Se_3$ crossbar heterostructure was implemented by Wang et al. (Figure 5a) [90]. The all-solution processed $MoSe_2/Bi_2Se_3$ nanosheets ensured a bipolar memory performance with low operating voltages under 790 nm of near-infrared (NIR) light illumination ranging from 0 to 1.65 $mW{\cdot}cm^{-2}$. The device showed stable performance within 10^6 s (Figure 5b) and 1000 consecutive cycles. PPF effect (Figure 5c) and ΔPSC with pulse number were demonstrated. Also, electrical-induced PPD followed optical-induced PPF (wavelength of 790 nm, intensity of 1 $mW{\cdot}cm^{-2}$) (Figure 5d). Figure 5e shows the working mechanism. When 790 nm of NIR is applied, photo-generated electrons are trapped in the hybrid $MoSe_2/Bi_2Se_3$ nanosheets while free holes combine with conductive Ag filaments, causing oxidation to Ag^+. Therefore, the current decreases, transiting to high resistive state (HRS). This PPD effect became stronger as the function of the light intensity increases. Therefore, the cartoon character image was demonstrated depending on the amount of light exposure, with shadow masks patterned differently by the pixels (Figure 5f,g).

In 2020, Zhai et al. proposed a phototransistor synapse device using an interesting optoelectronic property of upconverting nanoparticles (UCNPs) (Figure 5h) [91]. This design of phototransistor included UCNPs such as lanthanide-doped $NaYF_4$ ($NaYF_4$:Yb^{3+}) and Er^{3+}. Not only does the band alignment of pentacene and MoS_2 induce separation of photo-excited electron-hole pairs from MoS_2 and create synaptic weight, but the device was also introduced with UPNCs acting as internal illumination sources, directly providing enough optical energy to create excitons within the MoS_2 layer (Figure 5i). Specifically, the energy band gap of Yb^{3+} is narrow enough to generate electron-hole pairs under irradiation of 980 nm wavelength in near infrared (NIR) range. Where external optical energy is given by NIR, optically created exciton transfers into Er^{3+} in device level, then drops straightly down from LUMO to HOMO level, secondly generating intense luminescence in visible wavelengths in result. These phased characteristics of radiative energy transfer upconversion (RETU) prolong the lifetime of transporting excitons up to the microsecond scale, thereby enhancing neuromorphic behavior along with the preexisting synaptic weight on the pentacene-MoS_2 interface. As a result, an optically induced LTP phenomenon was created (Figure 5j). For the demonstration of optically induced LTP, an 11 × 11 pixels array of phototransistors was trained 15,000 times with mapping images of letters "N" and "A" and resulted in 70% recognition accuracy, solely under NIR luminescence (Figure 5k).

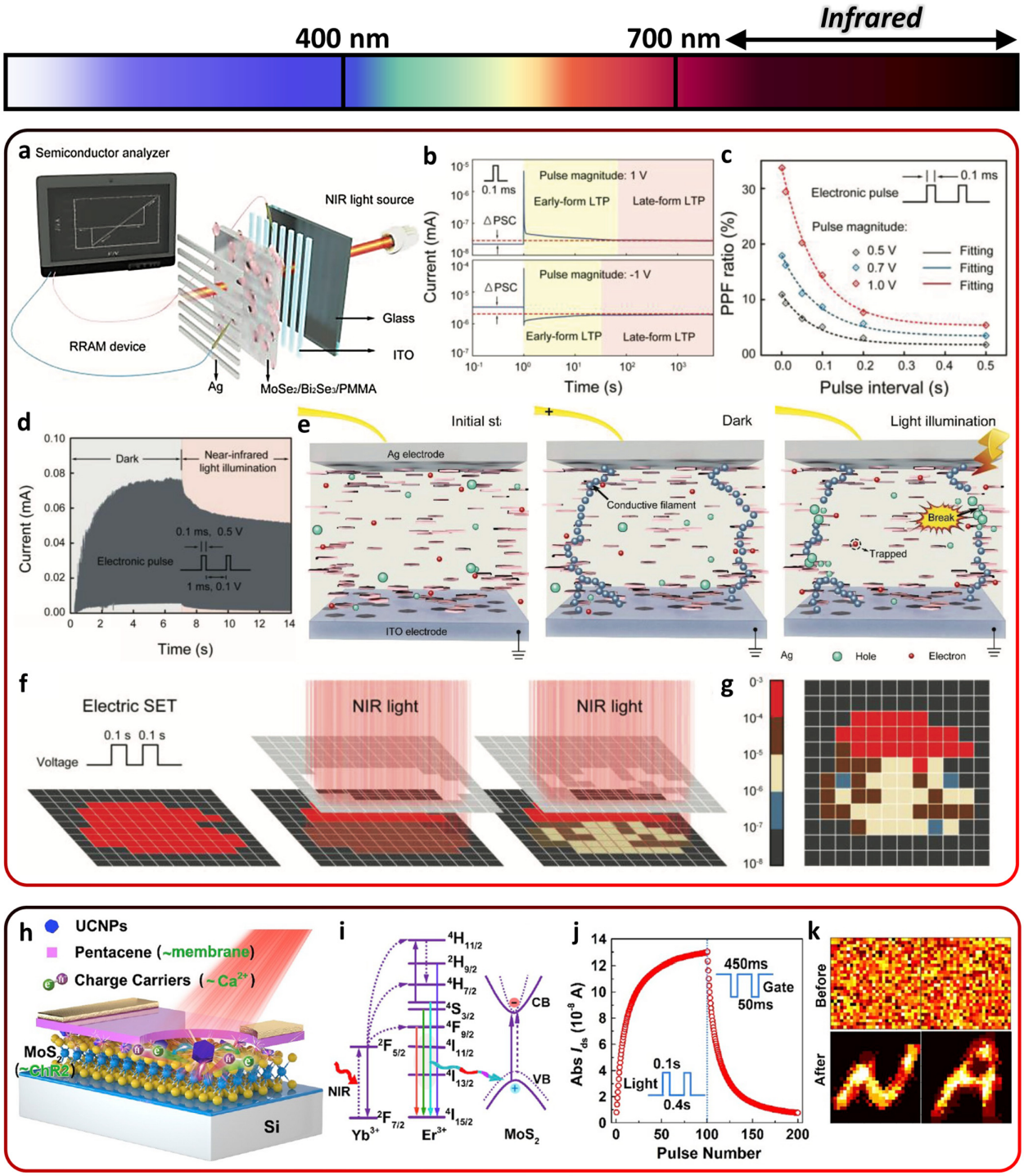

Figure 5. (**a**) Schematic illustration of the NIR light-modulated RRAM device. (**b**) EPSC by a single electronic pulse and IPSC by the −1 V electronic pulse from presynaptic terminal. (**c**) PPF behavior between two consecutive presynaptic pulses. (**d**) Experimental modulation of the NIR light on the memory device, which turns the PPF effect into PPD effect. (light wavenumber: 790 nm; light intensity: 1 mW·cm^{-2}). (**e**) Schematic illustration of a resistive switching model including initial state, Ag filaments formation, and filament rupture under light irradiation. (**f**) Schematic illustration image recognition of the RRAM array by NIR light. (**g**) Image demonstration by information storage operation of RRAM array. (**h**) A schematic illustration of pentacene/UPNPs/MoS_2 synaptic phototransistor. (**i**) An upconversion charge transfer from UCNPs NIR absorption to MoS_2 visible light detection.

(**j**) Optically induced LTP and electrically induced LTD. (**k**) Image recognizing demonstration of the upconversion phototransistor. (**a**–**g**) Reproduced with permission from [90]. Copyright Wiley, 2019. (**h**–**k**) Reproduced with permission from [91]. Copyright Elsevier, 2019.

3.4. Optoelectronic Neuromorphic Devices Using Multiple Wavelengths

In 2021, Hou et al. proposed a wafer-scale two-terminal flexible optoelectronic neuromorphic device with pyrenyl graphdiyne/graphene/PbS QDs, integrating an image sensor, memory, and visual neuromorphic devices in a single system (Figure 6a) [92]. They emulated excitatory and inhibitory synaptic behaviors both in an optical pathway by irradiating light of 450 nm and 980 nm, respectively, at Vg = 0 V. Compared to the dark state (Figure 6b(I)), Pyr-GDY film absorbs incident light of 450 nm and traps photo-generated holes, while electrons flow to the p-type channel of graphene (Figure 6b(II)). Therefore, the conductance decreases by capacitive coupling. On the other hand, PbS QDs mainly absorb light of 980 nm, capturing photo-generated electrons (Figure 6b(III)). Therefore, EPSC and IPSC could be selectively triggered by applying either 980 nm (500 $mW \cdot cm^{-2}$, 500 ms) or 450 nm (30 $mW \cdot cm^{-2}$, 500 ms), respectively (Figure 6c). The device showed reliable and robust LTP behaviors even after multiple bending tests (Figure 6d). A recognition rate higher than 80% was obtained with unfolded state of handwritten digits, suggesting the feasibility for wearable neuromorphic devices (Figure 6e).

Shan et al. developed a plasmonic optoelectronic memristor (Figure 6f) for neuromorphic vision in their 2022 research [93]. Sandwiching a TiO_2 layer between a Au top electrode and a FTO bottom electrode, Ag nanoparticles were mixed into the TiO_2 layer, taking the role of conducting filament in other typical memristor structures. The quantity of the conducting material can decide the effective diameter of the filament, also affecting the total resistance through the device. A schematic illustration of photo-induced redox is shown in Figure 6g. While the optical energy of visible light is not sufficient to generate excitons in TiO_2, gradual photooxidation of Ag nanoparticles into Ag^+ can occur with irradiation at this range of wavelength. Ag^+ creates a filament with superior conductivity in electrically driven memristor structure. Hence, visible light of 532 nm induced LTP with photooxidation (Figure 6h). Reversely, UV light of 360 nm wavelength has larger optical energy to directly generate excitons within TiO_2. Photo-excited electron-hole pairs at Ag/surface release electrons into the Ag conduction band, promoting the photoreduction process of Ag^+. The conversion of Ag^+ into the form of original Ag nanoparticles hinders the growth of the conducting filament under voltage pulse, eventually decreasing vertical current flow between the electrodes, hence creating a LTD effect (Figure 6i). This fully optical modulation of synaptic behavior was then used to demonstrate visual sensing and pre-processing of the output image with more than one wavelength (Figure 6j), where it showed effects of contrast enhancing and noise reducing functions of visible and UV light on this device, respectively.

In 2019, Li et al. presented a hetero-structured device of which the neuromorphic behavior can be modulated using a fully photonic method with lights of different wavelengths (Figure 6k) [94]. ZnO, with its naturally existing oxygen vacancy, absorbs and generates charge carriers under UV light illumination and ionizes oxygen vacancy into a charged state. These increases in ionized oxygen quantity can later induce creation of conductive filament with the help of positive charge to the top electrode, forcing the positively charged oxygen atoms to drift towards the bottom electrode and create a gradual current increase (Figure 6l). In the other hand, horizontally existing Pbs in the middle of the ZnO layer can absorb IR wavelength, which is neglected by ZnO, generating another set of excitons by Pbs itself. These sets of photoexcited electron-hole pairs can supply electrons to positively charged oxygen atoms from ZnO UV absorption, recombine, and cause a decrease in current through the vertical path between the electrodes (Figure 6m). Hence, illumination of 365 nm UV or 980 nm IR light to the device gained similar effects with applying positive or negative voltage, with the Pbs layer performing photon modulated floating gate. Due to a mutually effecting characteristic of ZnO and Pbs optoelectrical

performance, the device shows a gradual rise and decay of resistance change, inducing LTP and LTD. A demonstration work was performed by 28 × 28 memristor array, comparing image sensing features with the electrical modulation, where photonic modulation had similar results in recognition of alphabetic letters (Figure 6n,o).

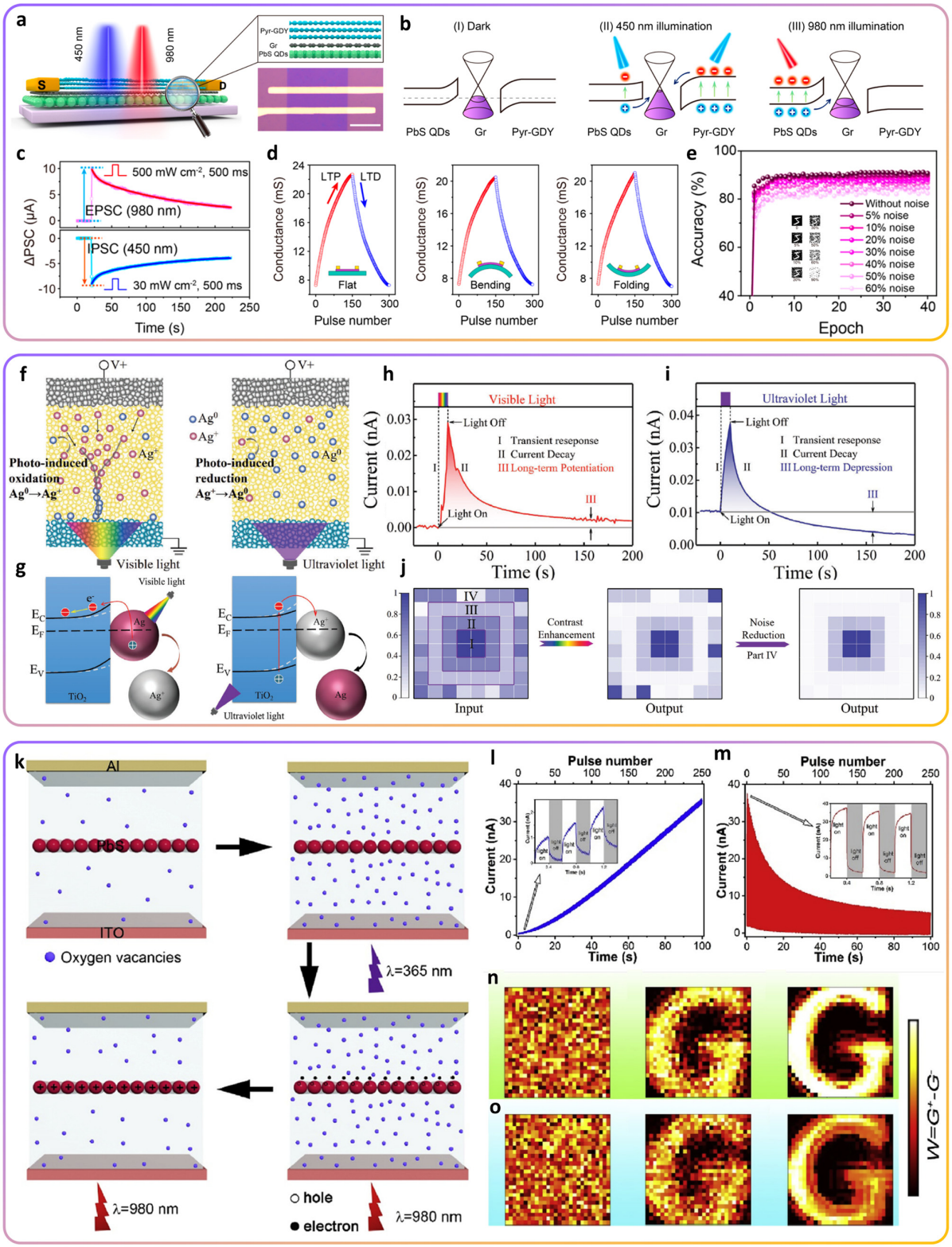

Figure 6. (**a**) Schematic illustration optoelectrical synaptic device based on the Pyr-GDY/Gr/PbS-QD heterostructure and its OM image. (**b**) Energy band alignment of the Pyr-GDY/Gr/PbS heterostructure

under (I) dark, (II) 450 nm illuminating, and (III) 980 nm illuminating condition. (**c**) EPSC and IPSC of the device induced by 980 and 450 nm optical pulses, respectively. (**d**) LTP and LTD behavior of the device after inducing potentiation and depression pulses under flat, bending, and folding conditions. (**e**) Recognition accuracy of the training epochs under the flat state. (**f**) Schematic illustrations of optically induced switching operation in Ag/TiO_2 photo-memristor device under visible and UV light. (**g**) An illustration of photo-induced redox reaction of Ag plasmonic particle. (**h**) LTP by visible light, and (**i**) LTD by UV light. (**j**) Demonstration of image contrast by visible light (irradiation intensity I: 1.0; II: 0.65; III: 0.32; IV: random, ranging from 0 to 0.75) and noise reduction by UV light on memristor array. (**k**) Optoelectronic neuromorphic operation of PbS/ZnO memristor with UV and IR light. (**l**) LTP and (**m**) LTD phenomena by UV and IR irradiation, respectively. (**n**) An image sensing demonstration of memristor array compared with an (**o**) electrical stimulation. (**a**–**e**) Reproduced with permission from [92]. Copyright American Chemical Society, 2020. (**f**–**j**) Reproduced with permission from [93]. Copyright Wiley, 2021. (**k**–**o**) Reproduced with permission from [94]. Copyright Elsevier, 2019.

In 2021, Huang et al. implemented an ambipolar synaptic phototransistor. Two-dimensional perovskite PEA_2SnI_4 and non-fullerene acceptor of Y6 were used as p-type and n-type material, respectively, forming a heterojunction. The device was fabricated on an indium tin oxide (ITO) glass substrate through solution process (Figure 7a,b) [95]. The absorption spectrums of PEA_2SnI_4 perovskite and Y6 are in the visible light and near-infrared (700 nm to 1000 nm) ranges, respectively, so the heterostructure extends its absorption spectrum from the visible to the NIR. The fabricated device was shown to simulate EPSC, IPSC, PPF, and STM/LTM synaptic functions by irradiating with NIR light of 808 nm and applying positive V_G (Figure 7c). The photo-generated holes from Y6 transited to PEA_2SnI_4, increasing drain current (I_{DS}). Meanwhile, electron-hole pairs were generated from both layers under visible light (450 nm, 520 nm, and 650 nm). The electrons were captured by the Sn vacancies in the perovskite film. The photogating effect reduced the I_{DS}, as hole carriers recombined with the electrons in channel. For the application, the 3×5 synaptic transistor array distinguished different colors of light, set to letter "G" (red), "o" (green), "o" (blue), and "d" (NIR), and showed memory characteristics on the order of tens of seconds (Figure 7d,e).

Zhang et al. presented a photoelectric synaptic transistor based on $CuInSe_2$ QDs in 2023, with the intention of mimicking the ion transfer between biological neuron cells as the schematic image of Figure 7f describes [96]. Under wide range irradiation throughout UV to IR, the transistor device generates electron-hole pairs originating from both $CuInSe_2$ QDs and P3HT layers. Where the band alignment is made in forms that traps electrons in $CuInSe_2$ and slides holes into P3HT, synaptic weight created by uneven distribution of negative and positive charge raises hole conductivity in P3HT, exhibiting gradual decay of the photocurrent, also with the aid of the PMMA layer slowing down carrier transfer between $CuInSe_2$ and P3HT (Figure 7g). Owing to the fact that the total light absorption in the device was largest in the UV wavelength and smallest in the IR wavelength (Figure 7h), the team rendered a fully light-controlled LTP and LTD, by switching stimuli from 365 nm to 850 nm optical pulse. Although lone use of 850 nm generates weak LTP phenomenon, adding 850 nm to the rapid decay after UV light stimuli extends photocurrent lifetime, synergistically creating clearer LTD behavior (Figure 7i).

Compared to existing single-channel optoelectronic neuromorphic devices, Cho et al. fabricated photonic neuro-transistors in 2019 [97]. With a CdS layer covering broadband light absorption from UV to visible and a ZTO layer providing high-mobility, a heterostructure was made to maximalize the advantages (Figure 7j). The high charge trap states in the CdS/ZTO interface achieved the high EPSC, STP/LTP and PPC behavior (Figure 7k). The PPC behavior is due to slowly de-trapping photo-generated carriers that were trapped at the defect sites in the CdS/ZTO interface when illuminating photonic spikes. Finally, Pavlov's associative learning was mimicked by using several optical pulses (Figure 7l). UV and visible light pulses were given for the compensation (food) and stimulation (bell),

respectively. After associative learning with UV light, bell ringing triggered salivation response with a PSC value above the threshold even without compensation (Figure 7m).

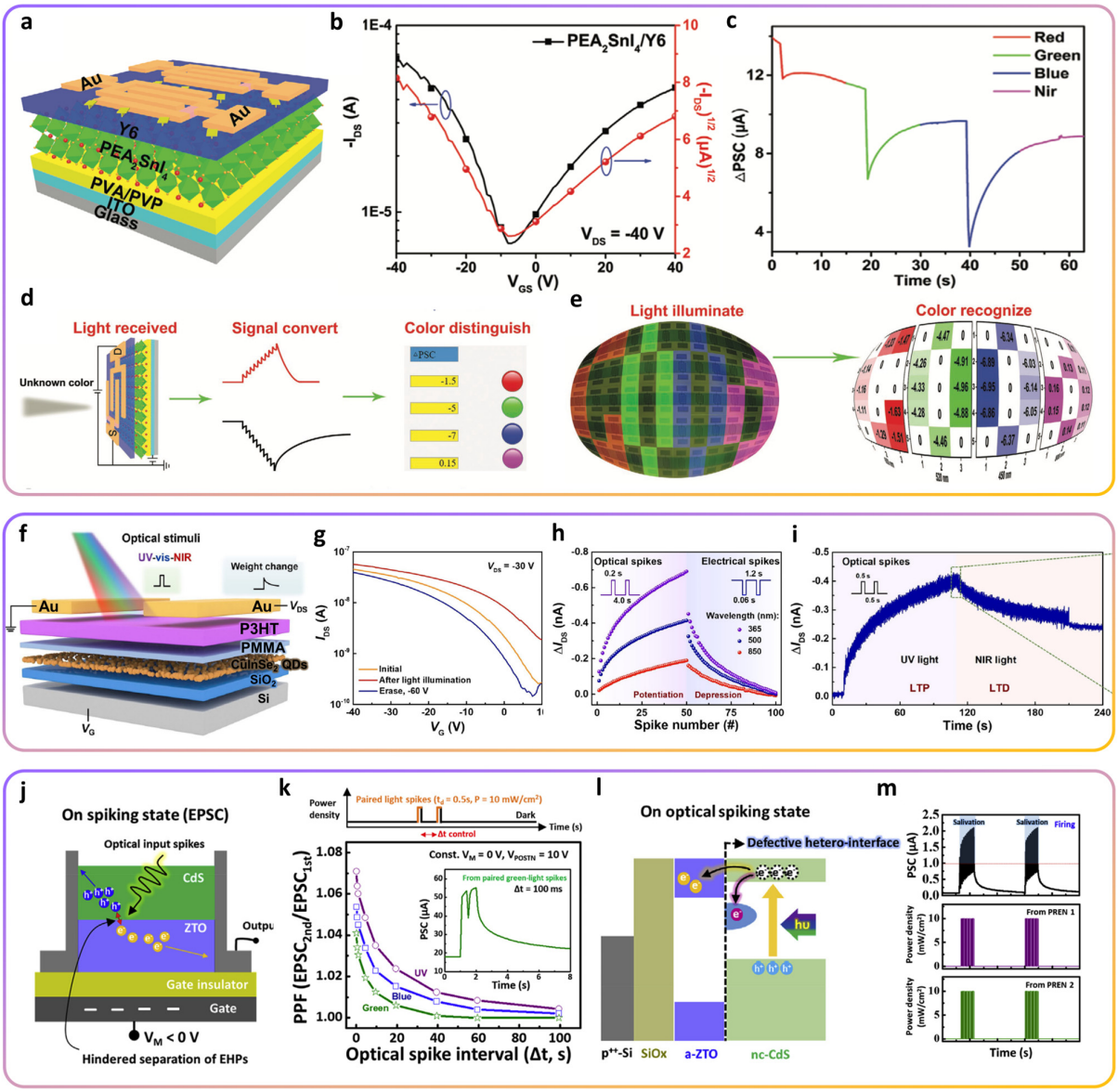

Figure 7. (**a**) A schematic illustration of phototransistors device structure based on PEA_2SnI_4 and Y6. (**b**) The transfer characteristics of the phototransistors in dark condition. (**c**) ΔPSC generated by red, green, blue, and NIR light with same optical intensity. (**d**) Simulation of unknown light recognition process of the synaptic transistor. (**e**) Input image of letter "G," "o," "o," and "d" by red, green, blue, and NIR LED light into the 12 × 5 transistor arrays and the output results of four 3 × 5 pixels. (**f**) A schematic illustration of neuron-mimicking phototransistor based on P3HT/PMMA/$CuInSe_2$ QDs. (**g**) Photo-induced writing state and electrical erase state of the device. (**h**) A comparison of potentiation and depression by illumination of 365 nm, 500 nm, 850 nm, respectively. (**i**) Optically modulated LTP and LTD by UV and NIR light. (**j**) A schematic illustration of modulation mechanism of Cds/ZTO based photo-synaptic transistor. (**k**) PPF behavior variation by interval time of green, blue, and UVpaired optical pulses. (**l**) The mechanism of photo-synaptic plasticity modulated by defective interface in CdS/ZTO heterostructure. (**m**) Fully-optical and multispectral modulation of learning process simulated by neuronal computation processing performance. (**a**–**e**) Reproduced with permission from [95]. Copyright Wiley, 2021. (**f**–**i**) Reproduced with permission from [96]. Copyright Wiley, 2023. (**j**–**m**) Reproduced with permission from [97]. Copyright Elsevier, 2019.

In 2022, Ni et al. demonstrated flexible organic-heterojunction neuromorphic transistor (OHNT) sensing broadband light from near-UV (NUV) to NIR, and processed multiplexed-neurotransmission signals for the first time [98]. PMMA, C8-BTBT, copper hexadecafluorophthalocyanine (F16CuPc), and PEN were used as dual-channel and flexible substrates. The device responded with different STM/LTM behaviors to 380 nm, 640 nm, and 790 nm light, respectively (Figure 8a). To utilize each wavelength-dependent response, a pain-perceptual receptor to sense NUV light was first realized with the OHNT (Figure 8b). Also, each EPSC state modulated by the interval 790 nm light pulses was converted to its corresponding International Morse code (Figure 8c). Finally, the letters of 'N', 'K', and 'U' were programmed with visible light. The optically programmed pattern lasted for 10 s, showing memory characteristics (Figure 8d).

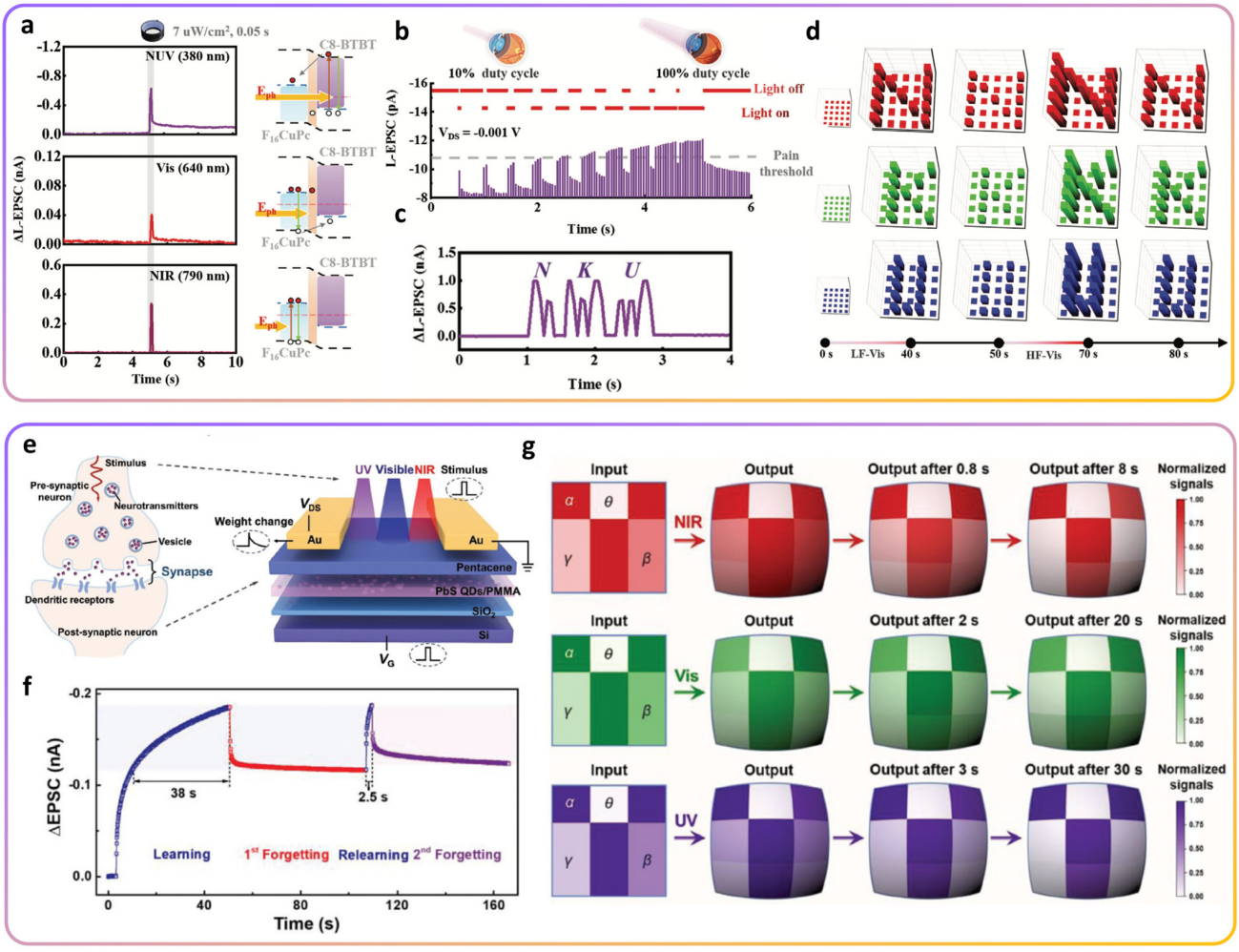

Figure 8. (**a**) ΔL-EPSCs for OHNT generated by 380, 640, and 790 nm illumination and energy band diagrams under the illuminations. (**b**) L-EPSCs generated by 380 nm UV light in variation of duty cycle. OHNT demonstration of (**c**) Morse code of "NKU" with 790 nm NIR light and (**d**) 5 × 5 pixel image of "NKU" 5 × 5 array with 640 nm light signals. (**e**) Retina-structured phototransistor based of pentacene/PbS QDs/PMMA. (**f**) Learning time difference between first and second learning processes. (**g**) Pattern recognizing demonstration by red, green, and blue light, respectively. (**a**–**d**) Reproduced with permission from [98]. Copyright Wiley, 2021. (**e**–**g**) Reproduced with permission from [99]. Copyright Wiley, 2023.

In 2023, Zhang et al. utilized another neuron-mimicking combination of QDs and p-type organic semiconductor, utilizing polymer-mixed PbS QDs and upper pentacene film layer for a human retina-like structure (Figure 8e) [99]. QDs were effectively captivated

in an insulating PMMA layer, which can slow down recombination of photo-generated excitons. Due to pentacene and Pbs QDs collecting holes and electrons, respectively, the charge separation weighs the band alignment down to a synaptic state. In addition to the advantage of exploiting wide-ranged absorption of the PbS QDs, the device showed the unique behavior of exhibiting significantly shorter rise time under secondly given optical stimulation (38 s to 2.4 s), mimicking the way the human brain tends to learn or memorize information faster with repetition of the same input even after seemingly forgetting the initial learning process (Figure 8f). The synaptic performance of the phototransistor was tested with pixel arrays with different intensity regions under 365 nm, 550 nm, and 850 nm wavelengths, resulting in clear pattern recognition in all three stimulations (Figure 8g).

4. Summary and Outlook

This review puts together neuromorphic and optoelectronic devices, providing a categorical insight on subdivision of stimuli energy level and structural designs. Based on this prospective, we revisited and sorted the recent research by means of utilized wavelength, as it can be roughly divided into UV, visible, and IR range, exhibiting diverse synaptic properties and various uses in artificial neural networks. Also, we believe categorizing devices with a distinct standard of countable terminal numbers gives this review a new perspective on comprehending boundlessly diverse neuromorphic devices, which are summarized in the following Table 1.

Table 1. Summary of heterostructure-based optoelectronic neuromorphic devices.

Structure	Material	Type	Bandgap (eV)	Wavelength (nm)	Application	Ref.
2-terminal	Graphene/PI	Inorganic/Organic	0.0	365	Image recognition	[80]
	4H-SiC/ P3HT	Inorganic/Organic	2.0/3.3	375	Image recognition	[81]
Transistor	ZnO/CdS	Inorganic	2.4/3.3	365	Image recognition	[58]
	ZnO NWs/ C8-BTBT	Inorganic/Organic	3.9/3.3	380	Image recognition	[82]
	BP/P_xO_x	Inorganic	0.3~1.0	365/280	Image recognition	[83]
	$CsPbBr_3$ QDs /Pentacene	Inorganic/Organic	1.8/2.8	365	N/A	[63]
	CDs/Silk protein	Inorganic/Organic	1.1/3.9~4.1	365	Image recognition	[84]
2-terminal	$CsPbI_2Br$/N-G QDs/ P3H	Inorganic/Organic	3.2/1.9/2.0	470	Image recognition	[85]
	NiO/CH-P	Inorganic/Organic	1.8	450/525/630	Color recognition	[86]
Transistor	PbS QDs/ P3HT/Si NM	Inorganic/Organic	0.8/2.0/1.12	532	Image recognition	[87]
	$CsPbBr_3$-QDs/ CNT	Inorganic	2.4/1.3	405	Image recognition	[88]
	$CsPbBr_3$ QDs/ DPP-DTT	Inorganic/Organic	2.3/1.7	450	Image recognition Logic	[89]
2-terminal	$MoSe_2/Bi_2Se_3$	Inorganic	1.5/4.2	790	Image recognition	[90]
Transistor	MoS_2/UC NPs/ Pentacene	Inorganic/Organic	1.7/1.8	980	Image recognition	[91]
2-terminal	PbS QDs/ pyrenyl graphdiyne	Inorganic/Organic	0.8/0.0/2.07	450/980	Image recognition	[92]
	TiO_2/Ag NPs	Inorganic	3.2/2.9	360/532	Image contrast Noise reduction	[93]
	PbS/ZnO	Inorganic	3.4/1.2	365/980	Image recognition	[94]

Table 1. *Cont.*

Structure	Material	Type	Bandgap (eV)	Wavelength (nm)	Application	Ref.
Transistor	PEA_2SnI_4/Y6	Inorganic/Organic	1.3/2.0	450/520/650 /808	Color recognition	[95]
	$CuInSe_2$ QDs/ P3HT	Inorganic/Organic	1.9/1.2	365/850	Image recognition	[96]
	CdS/ZTO	Inorganic	2.3/3.9	365/465/525	Pavlov's learning simulation	[97]
Transistor	C8-BTBT/ F16CuPc	Organic	1.5/3.7	380/640/790	Image recognition	[98]
	PbS QDs/ Pentacene	Inorganic/Organic	1.8/0.9	365/550/850	Image recognition	[99]

While the aforementioned studies exploited various materials and methods to render optoelectronic neuromorphic behaviors out of electronic devices, we determined aspects that need to be further developed from the currently reported states. First, lack of utilization of IR-ranged light was prominent in the general groups of synaptic devices, due to the lack of available IR-absorbing semiconductor materials. Light in IR wavelengths has high usability in medical and biological application, due to its harmless property derived from low optical energy, which can be safely applied to wearable and near-human devices. For the recent trend of biological applications of electronics, we believe that IR wavelength can be explored further in neuromorphic fields. Second, realization of optically modulated LTD phenomenon was scarcely reported, while LTP by solely optical methods was relatively commonly observed in many studies with optoelectronic neuromorphic topics. Gradual erasing of input information, or in other words, recovery from stimulation, is another unneglectable branch of information processing in human brain function, which requests researchers to further develop organic methods for the next steps in optoelectronic neuromorphic science.

Despite the remaining issues and challenges to overcome in emulating the work of biological neurons, the pure potential of neuromorphic behavior in electronic devices is extremely high. Especially in optical purpose, valuable applicational demands such as image sensing and artificial vision require further development in the field, as we also expect the merging of optoelectronic and neuromorphic domains to hold strong synergetic power, potentially leading to rapid expansion in mutual fields of application.

Author Contributions: H.Y. initiated the research project. J.P. and J.S. performed the literature survey and research analysis. All authors have read and agreed to the published version of the manuscript.

Funding: This research was supported by the National Research Foundation of Korea (NRF) grant funded by the Korean Government (MSIT) (NRF-2022R1C1C1004590) and the Gachon University research fund of 2023 (GCU-202303810001).

Data Availability Statement: The data presented in this study are available in this article.

Conflicts of Interest: The authors declare no conflicts of interest.

References

1. Elson, R.C.; Selverston, A.I.; Huerta, R.; Rulkov, N.F.; Rabinovich, M.I.; Abarbanel, H.D. Synchronous behavior of two coupled biological neurons. *Phys. Rev. Lett.* **1998**, *81*, 5692. [CrossRef]
2. Liu, Y.; Xu, W.-j.; Ma, J.; Alzahrani, F.; Hobiny, A. A new photosensitive neuron model and its dynamics. *Front. Inf. Technol. Electron. Eng.* **2020**, *21*, 1387–1396. [CrossRef]
3. Harikesh, P.C.; Yang, C.-Y.; Tu, D.; Gerasimov, J.Y.; Dar, A.M.; Armada-Moreira, A.; Massetti, M.; Kroon, R.; Bliman, D.; Olsson, R. Organic electrochemical neurons and synapses with ion mediated spiking. *Nat. Commun.* **2022**, *13*, 901. [CrossRef] [PubMed]
4. Zhu, J.; Zhang, T.; Yang, Y.; Huang, R. A comprehensive review on emerging artificial neuromorphic devices. *Appl. Phys. Rev.* **2020**, *7*, 011312. [CrossRef]

5. Milano, G.; Pedretti, G.; Fretto, M.; Boarino, L.; Benfenati, F.; Ielmini, D.; Valov, I.; Ricciardi, C. Brain-inspired structural plasticity through reweighting and rewiring in multi-terminal self-organizing memristive nanowire networks. *Adv. Intell. Syst.* **2020**, *2*, 2000096. [CrossRef]
6. Keene, S.T.; Lubrano, C.; Kazemzadeh, S.; Melianas, A.; Tuchman, Y.; Polino, G.; Scognamiglio, P.; Cinà, L.; Salleo, A.; van de Burgt, Y. A biohybrid synapse with neurotransmitter-mediated plasticity. *Nat. Mater.* **2020**, *19*, 969–973. [CrossRef]
7. Wei, H.; Ni, Y.; Sun, L.; Yu, H.; Gong, J.; Du, Y.; Ma, M.; Han, H.; Xu, W. Flexible electro-optical neuromorphic transistors with tunable synaptic plasticity and nociceptive behavior. *Nano Energy* **2021**, *81*, 105648. [CrossRef]
8. Tian, G.L.; Bi, J.S.; Xu, G.B.; Xi, K.; Xu, Y.N.; Yang, X.Q.; Yin, H.X.; Xu, Q.X.; Li, Y.L. $Hf_{0.5}Zr_{0.5}O_2$-based ferroelectric bionic electronic synapse device with highly symmetrical and linearity weight modification. *Electron. Lett.* **2020**, *56*, 840–843. [CrossRef]
9. Jung, W.; Yoon, J.; Ji, S.; Choi, J.Y.; Kim, J.M.; Nam, Y.; Kim, E.Y.; Lee, J. Exploring linearity of deep neural network trained QSM: QSMnet+. *Neuroimage* **2020**, *211*, 116619. [CrossRef]
10. Yang, S.T.; Li, X.Y.; Yu, T.L.; Wang, J.; Fang, H.; Nie, F.; He, B.; Zhao, L.; Lü, W.M.; Yan, S.S. High-Performance Neuromorphic Computing Based on Ferroelectric Synapses with Excellent Conductance Linearity and Symmetry. *Adv. Funct. Mater.* **2022**, *32*, 2202366. [CrossRef]
11. Hao, Y.; Huang, X.; Dong, M.; Xu, B. A biologically plausible supervised learning method for spiking neural networks using the symmetric STDP rule. *Neural Netw.* **2020**, *121*, 387–395. [CrossRef]
12. Wang, K.; Li, L.; Zhao, R.; Zhao, J.; Zhou, Z.; Wang, J.; Wang, H.; Tang, B.; Lu, C.; Lou, J. A pure 2H-MoS_2 nanosheet-based memristor with low power consumption and linear multilevel storage for artificial synapse emulator. *Adv. Electron. Mater.* **2020**, *6*, 1901342. [CrossRef]
13. Lee, Y.; Liu, Y.; Seo, D.-G.; Oh, J.Y.; Kim, Y.; Li, J.; Kang, J.; Kim, J.; Mun, J.; Foudeh, A.M. A low-power stretchable neuromorphic nerve with proprioceptive feedback. *Nat. Biomed. Eng.* **2023**, *7*, 511–519. [CrossRef]
14. Wang, T.-Y.; Meng, J.-L.; Rao, M.-Y.; He, Z.-Y.; Chen, L.; Zhu, H.; Sun, Q.-Q.; Ding, S.-J.; Bao, W.-Z.; Zhou, P. Three-dimensional nanoscale flexible memristor networks with ultralow power for information transmission and processing application. *Nano Lett.* **2020**, *20*, 4111–4120. [CrossRef]
15. Li, X.; Tang, J.; Zhang, Q.; Gao, B.; Yang, J.J.; Song, S.; Wu, W.; Zhang, W.; Yao, P.; Deng, N. Power-efficient neural network with artificial dendrites. *Nat. Nanotechnol.* **2020**, *15*, 776–782. [CrossRef]
16. Shin, H.; Jeong, S.; Lee, J.-H.; Sun, W.; Choi, N.; Cho, I.-J. 3D high-density microelectrode array with optical stimulation and drug delivery for investigating neural circuit dynamics. *Nat. Commun.* **2021**, *12*, 492. [CrossRef]
17. Wu, Q.; Dang, B.; Lu, C.; Xu, G.; Yang, G.; Wang, J.; Chuai, X.; Lu, N.; Geng, D.; Wang, H. Spike encoding with optic sensory neurons enable a pulse coupled neural network for ultraviolet image segmentation. *Nano Lett.* **2020**, *20*, 8015–8023. [CrossRef]
18. Zhang, H.; Thompson, J.; Gu, M.; Jiang, X.D.; Cai, H.; Liu, P.Y.; Shi, Y.; Zhang, Y.; Karim, M.F.; Lo, G.Q. Efficient on-chip training of optical neural networks using genetic algorithm. *Acs Photonics* **2021**, *8*, 1662–1672. [CrossRef]
19. Gao, Z.; Ju, X.; Zhang, H.; Liu, X.; Chen, H.; Li, W.; Zhang, H.; Liang, L.; Cao, H. InP Quantum Dots Tailored Oxide Thin Film Phototransistor for Bioinspired Visual Adaptation. *Adv. Funct. Mater.* **2023**, *33*, 2305959. [CrossRef]
20. Wan, C.; Cai, P.; Guo, X.; Wang, M.; Matsuhisa, N.; Yang, L.; Lv, Z.; Luo, Y.; Loh, X.J.; Chen, X. An artificial sensory neuron with visual-haptic fusion. *Nat. Commun.* **2020**, *11*, 4602. [CrossRef] [PubMed]
21. Wang, Z.; Zhu, L.; Zhang, H.; Li, G.; Yi, C.; Li, Y.; Yang, Y.; Ding, Y.; Zhen, M.; Gao, S. Real-time volumetric reconstruction of biological dynamics with light-field microscopy and deep learning. *Nat. Methods* **2021**, *18*, 551–556. [CrossRef]
22. Subin, P.; Midhun, P.; Antony, A.; Saji, K.; Jayaraj, M. Optoelectronic synaptic plasticity mimicked in ZnO-based artificial synapse for neuromorphic image sensing application. *Mater. Today Commun.* **2022**, *33*, 104232. [CrossRef]
23. Austin, E.; Geisler, A.N.; Nguyen, J.; Kohli, I.; Hamzavi, I.; Lim, H.W.; Jagdeo, J. Visible light. Part I: Properties and cutaneous effects of visible light. *J. Am. Acad. Dermatol.* **2021**, *84*, 1219–1231. [CrossRef]
24. Park, Y.; Roth, J.; Oka, D.; Hirose, Y.; Hasegawa, T.; Paul, A.; Pogrebnyakov, A.; Gopalan, V.; Birol, T.; Engel-Herbert, R. $SrNbO_3$ as a transparent conductor in the visible and ultraviolet spectra. *Commun. Phys.* **2020**, *3*, 102. [CrossRef]
25. Mokbel, H.; Graff, B.; Dumur, F.; Lalevée, J. NIR sensitizer operating under long wavelength (1064 nm) for free radical photopolymerization processes. *Macromol. Rapid Commun.* **2020**, *41*, 2000289. [CrossRef]
26. Mohania, D.; Chandel, S.; Kumar, P.; Verma, V.; Digvijay, K.; Tripathi, D.; Choudhury, K.; Mitten, S.K.; Shah, D. Ultraviolet radiations: Skin defense-damage mechanism. *Ultrav. Light Hum. Health Dis. Environ.* **2017**, *996*, 71–87.
27. Selvam, K.; Sivapragasam, S.; Poon, G.M.; Wyrick, J.J. Detecting recurrent passenger mutations in melanoma by targeted UV damage sequencing. *Nat. Commun.* **2023**, *14*, 2702. [CrossRef]
28. Kim, J.J.; Andrew, T.L. Real-time and noninvasive detection of UV-Induced deep tissue damage using electrical tattoos. *Biosens. Bioelectron.* **2020**, *150*, 111909. [CrossRef]
29. Panuski, C.; Englund, D.; Hamerly, R. Fundamental thermal noise limits for optical microcavities. *Phys. Rev. X* **2020**, *10*, 041046. [CrossRef]
30. Guan, J.; Lai, R.; Xiong, A.; Liu, Z.; Gu, L. Fixed pattern noise reduction for infrared images based on cascade residual attention CNN. *Neurocomputing* **2020**, *377*, 301–313. [CrossRef]
31. Al-Said, S.M.; Abu-Nabah, B.A. Physics-based thermal noise effect reduction in sonic IR crack length estimation. *Nondestruct. Test. Eval.* **2023**, 1–22. [CrossRef]

32. Lee, S.; Park, T.; Hur, J.; Yoo, H. Calcium Titanate Orthorhombic Perovskite-Nickel Oxide Solar-Blind UVC Photodetectors with Unprecedented Long-Term Stability Exceeding 500 Days and Their Applications to Real-Time Flame Detection. *ACS Photonics* **2022**, *9*, 4005–4016. [CrossRef]
33. Choi, W.; Park, T.; Yoo, H.; Hur, J. Vertical asymmetric metal-semiconductor-metal photodiode based on β-Ga_2O_3 thin films fabricated via solution process for arc discharge detection. *J. Alloys Compd.* **2023**, *953*, 170169. [CrossRef]
34. Hong, S.; Zagni, N.; Choo, S.; Liu, N.; Baek, S.; Bala, A.; Yoo, H.; Kang, B.H.; Kim, H.J.; Yun, H.J. Highly sensitive active pixel image sensor array driven by large-area bilayer MoS_2 transistor circuitry. *Nat. Commun.* **2021**, *12*, 3559. [CrossRef]
35. Zhang, Y.; Wang, Q.; Liu, D.; Wang, Q.; Li, T.; Wang, Z. Cu_2O-BiOI isotype (pp) heterojunction: Boosted visible-light-driven photoelectrochemical activity for non-enzymatic H_2O_2 sensing. *Appl. Surf. Sci.* **2020**, *521*, 146434. [CrossRef]
36. Narang, N.; Bourlai, T. Classification of soft biometric traits when matching near-infrared long-range face images against their visible counterparts. *Secur. Soc. Identity Mob. Platf. Technol. Secur. Priv. Identity Manag.* **2020**, 77–104.
37. Kwan, C.; Larkin, J. Detection of small moving objects in long range infrared videos from a change detection perspective. *Photonics* **2021**, *8*, 394. [CrossRef]
38. Pupeza, I.; Huber, M.; Trubetskov, M.; Schweinberger, W.; Hussain, S.A.; Hofer, C.; Fritsch, K.; Poetzlberger, M.; Vamos, L.; Fill, E. Field-resolved infrared spectroscopy of biological systems. *Nature* **2020**, *577*, 52–59. [CrossRef] [PubMed]
39. Jose, D.A.; Sakla, R.; Sharma, N.; Gadiyaram, S.; Kaushik, R.; Ghosh, A. Sensing and bioimaging of the gaseous signaling molecule hydrogen sulfide by near-infrared fluorescent probes. *ACS Sens.* **2020**, *5*, 3365–3391. [CrossRef]
40. Zhang, N.-N.; Lu, C.-Y.; Chen, M.-J.; Xu, X.-L.; Shu, G.-F.; Du, Y.-Z.; Ji, J.-S. Recent advances in near-infrared II imaging technology for biological detection. *J. Nanobiotechnol.* **2021**, *19*, 132. [CrossRef]
41. Liang, S.J.; Cheng, B.; Cui, X.; Miao, F. Van der Waals heterostructures for high-performance device applications: Challenges and opportunities. *Adv. Mater.* **2020**, *32*, 1903800. [CrossRef]
42. Ahmad, W.; Liu, J.; Jiang, J.; Hao, Q.; Wu, D.; Ke, Y.; Gan, H.; Laxmi, V.; Ouyang, Z.; Ouyang, F. Strong Interlayer Transition in Few-Layer InSe/$PdSe_2$ van der Waals Heterostructure for Near-Infrared Photodetection. *Adv. Funct. Mater.* **2021**, *31*, 2104143. [CrossRef]
43. Singh, A.K.; Ahn, K.; Yoo, D.; Lee, S.; Ali, A.; Yi, G.-C.; Chung, K. van der Waals integration of GaN light-emitting diode arrays on foreign graphene films using semiconductor/graphene heterostructures. *NPG Asia Mater.* **2022**, *14*, 57. [CrossRef]
44. Afzal, A.M.; Iqbal, M.Z.; Mumtaz, S.; Akhtar, I. Multifunctional and high-performance GeSe/$PdSe_2$ heterostructure device with a fast photoresponse. *J. Mater. Chem. C* **2020**, *8*, 4743–4753. [CrossRef]
45. Qi, T.; Gong, Y.; Li, A.; Ma, X.; Wang, P.; Huang, R.; Liu, C.; Sakidja, R.; Wu, J.Z.; Chen, R. Interlayer transition in a vdW heterostructure toward ultrahigh detectivity shortwave infrared photodetectors. *Adv. Funct. Mater.* **2020**, *30*, 1905687. [CrossRef]
46. Pi, L.; Wang, P.; Liang, S.-J.; Luo, P.; Wang, H.; Li, D.; Li, Z.; Chen, P.; Zhou, X.; Miao, F. Broadband convolutional processing using band-alignment-tunable heterostructures. *Nat. Electron.* **2022**, *5*, 248–254. [CrossRef]
47. Wang, C.-Y.; Liang, S.-J.; Wang, S.; Wang, P.; Li, Z.A.; Wang, Z.; Gao, A.; Pan, C.; Liu, C.; Liu, J. Gate-tunable van der Waals heterostructure for reconfigurable neural network vision sensor. *Sci. Adv.* **2020**, *6*, eaba6173. [CrossRef]
48. Wang, Z.; Hemmetter, A.; Uzlu, B.; Saeed, M.; Hamed, A.; Kataria, S.; Negra, R.; Neumaier, D.; Lemme, M.C. Graphene in 2D/3D heterostructure diodes for high performance electronics and optoelectronics. *Adv. Electron. Mater.* **2021**, *7*, 2001210. [CrossRef]
49. Stanev, T.K.; Liu, P.; Zeng, H.; Lenferink, E.J.; Murthy, A.A.; Speiser, N.; Watanabe, K.; Taniguchi, T.; Dravid, V.P.; Stern, N.P. Direct Patterning of Optoelectronic Nanostructures Using Encapsulated Layered Transition Metal Dichalcogenides. *ACS Appl. Mater. Interfaces* **2022**, *14*, 23775–23784. [CrossRef]
50. Cerrillo, J.G.; Distler, A.; Matteocci, F.; Forberich, K.; Wagner, M.; Basu, R.; Castriotta, L.A.; Jafarzadeh, F.; Brunetti, F.; Yang, F. Matching the photocurrent of 2-terminal mechanically-stacked perovskite/organic tandem solar modules by varying the cell width. *Sol. RRL* **2023**, *8*, 2300767. [CrossRef]
51. Nguyen, D.C.; Sato, K.; Hamada, M.; Murata, F.; Ishikawa, Y. Annual output energy harvested by building-integrated photovoltaics based on the optimized structure of 2-terminal perovskite/silicon tandem cells under realistic conditions. *Sol. Energy* **2022**, *241*, 452–459. [CrossRef]
52. Bellucci, A.; García-Linares, P.; Martí, A.; Trucchi, D.M.; Datas, A. A three-terminal hybrid thermionic-photovoltaic energy converter. *Adv. Energy Mater.* **2022**, *12*, 2200357. [CrossRef]
53. O'Donnell, C. Nonlinear slow-timescale mechanisms in synaptic plasticity. *Curr. Opin. Neurobiol.* **2023**, *82*, 102778. [CrossRef]
54. Abbott, L.F.; Nelson, S.B. Synaptic plasticity: Taming the beast. *Nat. Neurosci.* **2000**, *3*, 1178–1183. [CrossRef]
55. Chen, X.; Chen, B.; Jiang, B.; Gao, T.; Shang, G.; Han, S.T.; Kuo, C.C.; Roy, V.A.; Zhou, Y. Nanowires for UV–vis–IR optoelectronic synaptic devices. *Adv. Funct. Mater.* **2023**, *33*, 2208807. [CrossRef]
56. Kim, J.; Kim, Y.; Kwon, O.; Kim, T.; Oh, S.; Jin, S.; Park, W.; Kwon, J.D.; Hong, S.W.; Lee, C.S. Modulation of Synaptic Plasticity Mimicked in Al Nanoparticle-Embedded IGZO Synaptic Transistor. *Adv. Electron. Mater.* **2020**, *6*, 1901072. [CrossRef]
57. Lin, C.Y.; Chen, J.; Chen, P.H.; Chang, T.C.; Wu, Y.; Eshraghian, J.K.; Moon, J.; Yoo, S.; Wang, Y.H.; Chen, W.C. Adaptive synaptic memory via lithium ion modulation in RRAM devices. *Small* **2020**, *16*, 2003964. [CrossRef]
58. Han, X.; Zhang, Y.; Huo, Z.; Wang, X.; Hu, G.; Xu, Z.; Lu, H.; Lu, Q.; Sun, X.; Qiu, L. A Two-Terminal Optoelectronic Synapses Array Based on the ZnO/Al_2O_3/CdS Heterojunction with Strain-Modulated Synaptic Weight. *Adv. Electron. Mater.* **2023**, *9*, 2201068. [CrossRef]

59. Culotta, L.; Penzes, P. Exploring the mechanisms underlying excitation/inhibition imbalance in human iPSC-derived models of ASD. *Mol. Autism* **2020**, *11*, 32.
60. Vinel, C.; Rosser, G.; Guglielmi, L.; Constantinou, M.; Pomella, N.; Zhang, X.; Boot, J.R.; Jones, T.A.; Millner, T.O.; Dumas, A.A. Comparative epigenetic analysis of tumour initiating cells and syngeneic EPSC-derived neural stem cells in glioblastoma. *Nat. Commun.* **2021**, *12*, 6130. [CrossRef]
61. Choi, Y.; Oh, S.; Qian, C.; Park, J.-H.; Cho, J.H. Vertical organic synapse expandable to 3D crossbar array. *Nat. Commun.* **2020**, *11*, 4595. [CrossRef]
62. Park, J.; Jang, Y.; Lee, J.; An, S.; Mok, J.; Lee, S.Y. Synaptic Transistor Based on In-Ga-Zn-O Channel and Trap Layers with Highly Linear Conductance Modulation for Neuromorphic Computing. *Adv. Electron. Mater.* **2023**, *9*, 2201306. [CrossRef]
63. Wang, Y.; Lv, Z.; Chen, J.; Wang, Z.; Zhou, Y.; Zhou, L.; Chen, X.; Han, S.T. Photonic synapses based on inorganic perovskite quantum dots for neuromorphic computing. *Adv. Mater.* **2018**, *30*, 1802883. [CrossRef]
64. France, G.; Volianskis, R.; Ingram, R.; Bannister, N.; Rothärmel, R.; Irvine, M.; Fang, G.; Burnell, E.; Sapkota, K.; Costa, B.M. Differential regulation of STP, LTP and LTD by structurally diverse NMDA receptor subunit-specific positive allosteric modulators. *Neuropharmacology* **2022**, *202*, 108840. [CrossRef]
65. Wang, Y.; Han, B.; Mayor, M.; Samorì, P. Opto-Electrochemical Synaptic Memory in Supramolecularly Engineered Janus 2D MoS_2. *Adv. Mater.* **2023**, *36*, 2307359. [CrossRef]
66. Ansari, M.H.R.; Kannan, U.M.; Cho, S. Core-shell dual-gate nanowire charge-trap memory for synaptic operations for neuromorphic applications. *Nanomaterials* **2021**, *11*, 1773. [CrossRef]
67. Mu, B.; Guo, L.; Liao, J.; Xie, P.; Ding, G.; Lv, Z.; Zhou, Y.; Han, S.T.; Yan, Y. Near-Infrared Artificial Synapses for Artificial Sensory Neuron System. *Small* **2021**, *17*, 2103837. [CrossRef] [PubMed]
68. Kim, M.K.; Lee, J.S. Synergistic improvement of long-term plasticity in photonic synapses using ferroelectric polarization in hafnia-based oxide-semiconductor transistors. *Adv. Mater.* **2020**, *32*, 1907826. [CrossRef] [PubMed]
69. Lee, K.-C.; Li, M.; Chang, Y.-H.; Yang, S.-H.; Lin, C.-Y.; Chang, Y.-M.; Yang, F.-S.; Watanabe, K.; Taniguchi, T.; Ho, C.-H. Inverse paired-pulse facilitation in neuroplasticity based on interface-boosted charge trapping layered electronics. *Nano Energy* **2020**, *77*, 105258. [CrossRef]
70. Yang, W.C.; Lin, Y.C.; Inagaki, S.; Shimizu, H.; Ercan, E.; Hsu, L.C.; Chueh, C.C.; Higashihara, T.; Chen, W.C. Low-Energy-Consumption and Electret-Free Photosynaptic Transistor Utilizing Poly (3-hexylthiophene)-Based Conjugated Block Copolymers. *Adv. Sci.* **2022**, *9*, 2105190. [CrossRef]
71. Sokolov, A.; Ali, M.; Li, H.; Jeon, Y.R.; Ko, M.J.; Choi, C. Partially oxidized MXene $Ti_3C_2T_x$ sheets for memristor having synapse and threshold resistive switching characteristics. *Adv. Electron. Mater.* **2021**, *7*, 2000866. [CrossRef]
72. Wang, Z.; Zeng, T.; Ren, Y.; Lin, Y.; Xu, H.; Zhao, X.; Liu, Y.; Ielmini, D. Toward a generalized Bienenstock-Cooper-Munro rule for spatiotemporal learning via triplet-STDP in memristive devices. *Nat. Commun.* **2020**, *11*, 1510. [CrossRef] [PubMed]
73. Walters, B.; Jacob, M.V.; Amirsoleimani, A.; Rahimi Azghadi, M. A Review of Graphene-Based Memristive Neuromorphic Devices and Circuits. *Adv. Intell. Syst.* **2023**, *5*, 2300136. [CrossRef]
74. Subin, P.; Asha, A.; Saji, K.; Jayaraj, M. Spike-dependent plasticity modulation in TiO_2-based synaptic device. *J. Mater. Sci. Mater. Electron.* **2021**, *32*, 13051–13061. [CrossRef]
75. Mannion, D.J.; Vu, V.C.; Ng, W.H.; Mehonic, A.; Kenyon, A.J. Unipolar potentiation and depression in memristive devices utilising the subthreshold regime. *IEEE Trans. Nanotechnol.* **2023**, *22*, 313–320. [CrossRef]
76. Hadiyal, K.; Ganesan, R.; Rastogi, A.; Thamankar, R. Bio-inspired artificial synapse for neuromorphic computing based on NiO nanoparticle thin film. *Sci. Rep.* **2023**, *13*, 7481. [CrossRef] [PubMed]
77. Farronato, M.; Mannocci, P.; Melegari, M.; Ricci, S.; Compagnoni, C.M.; Ielmini, D. Reservoir computing with charge-trap memory based on a MoS_2 channel for neuromorphic engineering. *Adv. Mater.* **2023**, *35*, 2205381. [CrossRef]
78. Yan, Y.; Li, J.C.; Chen, Y.T.; Wang, X.Y.; Cai, G.R.; Park, H.W.; Kim, J.H.; Zhao, J.S.; Hwang, C.S. Area-Type Electronic Bipolar Switching $Al/TiO_{1.7}/TiO_2/Al$ Memory with Linear Potentiation and Depression Characteristics. *ACS Appl. Mater. Interfaces* **2021**, *13*, 39561–39572. [CrossRef]
79. Shao, Z.-Y.; Huang, H.-M.; Guo, X. Optimizing linearity of weight updating in TaOx-based memristors by depression pulse scheme for neuromorphic computing. *Solid State Ion.* **2021**, *370*, 115746. [CrossRef]
80. Guo, J.; Yuan, X.; Ruan, H.; Duan, Y.; Liu, Y.; Kong, C.; Liu, Y.; Su, M.; Xie, T.; Wang, H. A flexible PI/graphene heterojunction optoelectronic device modulated by TENG and UV light for neuromorphic vision system. *Nano Energy* **2023**, *117*, 108928. [CrossRef]
81. Liu, X.; Huang, W.; Kai, C.; Yin, L.; Wang, Y.; Liu, X.; Pi, X.; Yang, D. Photogated Synaptic Transistors Based on the Heterostructure of 4H-SiC and Organic Semiconductors for Neuromorphic Ultraviolet Vision. *ACS Appl. Electron. Mater.* **2023**, *5*, 367–374. [CrossRef]
82. Ni, Y.; Zhang, S.; Sun, L.; Liu, L.; Wei, H.; Xu, Z.; Xu, W.; Xu, W. A low-dimensional hybrid pin heterojunction neuromorphic transistor with ultra-high UV sensitivity and immediate switchable plasticity. *Appl. Mater. Today* **2021**, *25*, 101223. [CrossRef]
83. Ahmed, T.; Tahir, M.; Low, M.X.; Ren, Y.; Tawfik, S.A.; Mayes, E.L.; Kuriakose, S.; Nawaz, S.; Spencer, M.J.; Chen, H. Fully Light-controlled memory and neuromorphic computation in layered black phosphorus. *Adv. Mater.* **2021**, *33*, 2004207. [CrossRef]
84. Lv, Z.; Chen, M.; Qian, F.; Roy, V.A.; Ye, W.; She, D.; Wang, Y.; Xu, Z.X.; Zhou, Y.; Han, S.T. Mimicking neuroplasticity in a hybrid biopolymer transistor by dual modes modulation. *Adv. Funct. Mater.* **2019**, *29*, 1902374. [CrossRef]

85. Zhang, S.; Zhao, Y.; Chen, Q.; Wang, Y.; Jiang, J.; Wang, Y.; Fu, Y.; Liu, Q.; Wang, Q.; He, D. A perovskite-based artificial photonic synapse with visible light modulation and ultralow current for neuromorphic computing. *Microelectron. Eng.* **2023**, *274*, 111982. [CrossRef]
86. Lee, J.; Jeong, B.H.; Kamaraj, E.; Kim, D.; Kim, H.; Park, S.; Park, H.J. Light-enhanced molecular polarity enabling multispectral color-cognitive memristor for neuromorphic visual system. *Nat. Commun.* **2023**, *14*, 5775. [CrossRef] [PubMed]
87. Wang, Y.; Yin, L.; Huang, S.; Xiao, R.; Zhang, Y.; Li, D.; Pi, X.; Yang, D. Silicon-Nanomembrane-Based Broadband Synaptic Phototransistors for Neuromorphic Vision. *Nano Lett.* **2023**, *23*, 8460–8467. [CrossRef]
88. Zhu, Q.-B.; Li, B.; Yang, D.-D.; Liu, C.; Feng, S.; Chen, M.-L.; Sun, Y.; Tian, Y.-N.; Su, X.; Wang, X.-M. A flexible ultrasensitive optoelectronic sensor array for neuromorphic vision systems. *Nat. Commun.* **2021**, *12*, 1798. [CrossRef]
89. Zhang, J.; Sun, T.; Zeng, S.; Hao, D.; Yang, B.; Dai, S.; Liu, D.; Xiong, L.; Zhao, C.; Huang, J. Tailoring neuroplasticity in flexible perovskite QDs-based optoelectronic synaptic transistors by dual modes modulation. *Nano Energy* **2022**, *95*, 106987. [CrossRef]
90. Wang, Y.; Yang, J.; Wang, Z.; Chen, J.; Yang, Q.; Lv, Z.; Zhou, Y.; Zhai, Y.; Li, Z.; Han, S.T. Near-infrared annihilation of conductive filaments in quasiplane MoSe2/Bi2Se3 nanosheets for mimicking heterosynaptic plasticity. *Small* **2019**, *15*, 1805431. [CrossRef]
91. Zhai, Y.; Zhou, Y.; Yang, X.; Wang, F.; Ye, W.; Zhu, X.; She, D.; Lu, W.D.; Han, S.-T. Near infrared neuromorphic computing via upconversion-mediated optogenetics. *Nano Energy* **2020**, *67*, 104262. [CrossRef]
92. Hou, Y.-X.; Li, Y.; Zhang, Z.-C.; Li, J.-Q.; Qi, D.-H.; Chen, X.-D.; Wang, J.-J.; Yao, B.-W.; Yu, M.-X.; Lu, T.-B. Large-scale and flexible optical synapses for neuromorphic computing and integrated visible information sensing memory processing. *ACS Nano* **2020**, *15*, 1497–1508. [CrossRef] [PubMed]
93. Shan, X.; Zhao, C.; Wang, X.; Wang, Z.; Fu, S.; Lin, Y.; Zeng, T.; Zhao, X.; Xu, H.; Zhang, X. Plasmonic Optoelectronic Memristor Enabling Fully Light-Modulated Synaptic Plasticity for Neuromorphic Vision. *Adv. Sci.* **2022**, *9*, 2104632. [CrossRef]
94. Li, H.; Jiang, X.; Ye, W.; Zhang, H.; Zhou, L.; Zhang, F.; She, D.; Zhou, Y.; Han, S.-T. Fully photon modulated heterostructure for neuromorphic computing. *Nano Energy* **2019**, *65*, 104000. [CrossRef]
95. Huang, X.; Li, Q.; Shi, W.; Liu, K.; Zhang, Y.; Liu, Y.; Wei, X.; Zhao, Z.; Guo, Y.; Liu, Y. Dual-Mode Learning of Ambipolar Synaptic Phototransistor Based on 2D Perovskite/Organic Heterojunction for Flexible Color Recognizable Visual System. *Small* **2021**, *17*, 2102820. [CrossRef] [PubMed]
96. Zhang, J.; Guo, Z.; Sun, T.; Guo, P.; Liu, X.; Gao, H.; Dai, S.; Xiong, L.; Huang, J. Energy-efficient organic photoelectric synaptic transistors with environment-friendly $CuInSe_2$ quantum dots for broadband neuromorphic computing. *SmartMat* **2023**, e1246. [CrossRef]
97. Cho, S.W.; Kwon, S.M.; Lee, M.; Jo, J.-W.; Heo, J.S.; Kim, Y.-H.; Cho, H.K.; Park, S.K. Multi-spectral gate-triggered heterogeneous photonic neuro-transistors for power-efficient brain-inspired neuromorphic computing. *Nano Energy* **2019**, *66*, 104097. [CrossRef]
98. Ni, Y.; Feng, J.; Liu, J.; Yu, H.; Wei, H.; Du, Y.; Liu, L.; Sun, L.; Zhou, J.; Xu, W. An artificial nerve capable of UV-perception, NIR–vis switchable plasticity modulation, and motion state monitoring. *Adv. Sci.* **2022**, *9*, 2102036. [CrossRef]
99. Zhang, J.; Guo, P.; Guo, Z.; Li, L.; Sun, T.; Liu, D.; Tian, L.; Zu, G.; Xiong, L.; Zhang, J. Retina-Inspired Artificial Synapses with Ultraviolet to Near-Infrared Broadband Responses for Energy-Efficient Neuromorphic Visual Systems. *Adv. Funct. Mater.* **2023**, *33*, 2302885. [CrossRef]